frontiers | Frontiers in Environmental Science

TYPE Original Research
PUBLISHED 26 August 2025
DOI 10.3389/fenvs.2025.1623548

OPEN ACCESS

EDITED BY
Williamson Gustave,
University of The Bahamas, Bahamas

REVIEWED BY
Mark Stephens,
University of The Bahamas, Bahamas
Iranzi Emile Rushimisha,
Shantou University, China

*CORRESPONDENCE
Chunjie Li,
lichunjie08@126.com

RECEIVED 06 May 2025
ACCEPTED 11 August 2025
PUBLISHED 26 August 2025

CITATION
Li C and Guo S (2025) Elevation-gradient patterns of soil microaggregate elemental distribution and chemical morphology in Tongbai Mountain, China's North–South climatic transition zone.
Front. Environ. Sci. 13:1623548.
doi: 10.3389/fenvs.2025.1623548

Elevation-gradient patterns of soil microaggregate elemental distribution and chemical morphology in Tongbai Mountain, China's North–South climatic transition zone

Chunjie Li[1]* and Shili Guo[2]

[1]School of Geographic Science and Tourism, Nanyang Normal University, Nanyang, China, [2]School of Economics, Southwestern University of Finance and Economics, Chengdu, China

Mountain-soil microaggregates play a crucial role in carbon storage and the transport of heavy metals. However, their biogeochemical behavior along elevation gradients is not well understood. In this study, we examine the chemistry of microaggregates from 200 m to 1,140 m on Tongbai Mountain, located in Central China. We employ a range of surface- and bulk-sensitive techniques, including X-ray photoelectron spectroscopy, scanning electron microscopy with energy-dispersive spectroscopy, X-ray fluorescence, Fourier-transform infrared spectroscopy, and X-ray diffraction. Our analysis reveals three distinct altitudinal regimes in elemental distribution. At low elevations (<600 m), microaggregate surfaces are enriched in Mn and Fe (XPS Mn up to 1.61% and Fe ≈ 3.37% at 200 m), reflecting exogenous inputs and reducing conditions that favour metal mobility. Mid-elevations soils (600–700 m) host elevated P and Al, signalling intense weathering and biological turnover in this transition zone. Above 700 m, cooler and wetter conditions promote the formation of organo-mineral complexes that sequester C, N and Fe; the C-N component in XPS spectra rises from 19.2% at 200 m to 26.4% at 1,140 m, while pyridinic-N increases from 21.1% to 44.4%. Concurrently, Fe^{3+} becomes the dominant iron species, consistent with enhanced humification and oxidative weathering at higher elevations. These trends point to an altitudinal threshold near 600–700 m. Below this break point, weaker organo-mineral associations allow greater heavy-metal mobility and carbon loss. Above it, robust complexes act as sinks for both carbon and metals, buffering soils against disturbance. Management should therefore be stratified: stringent pollution controls at low elevations, vegetation reinforcement on mid-slopes and conservation of high-elevation refugia. Our findings provide a mechanistic framework for mountain soil stewardship under global change. Projected warming and altered precipitation are likely to intensify metal leaching at lower elevations while underscoring the role of high-elevation soils as critical reservoirs for carbon and metal retention within China's north–south climatic transition zone.

KEYWORDS

vertical band spectrum, soil microaggregates, elemental chemical forms, organic-mineral complexes, biogeochemical processes, Tongbai Mountain

1 Introduction

As an important component of the Earth's key belts, mountain ecosystems play an irreplaceable role in regulating biogeochemical processes with their unique vertical belt spectrum characteristics (Kuzyakov and Blagodatskaya, 2015; Nottingham et al., 2018). In the context of global climate change and increasing human activity, mountain soils have become not only important carbon sink carriers, but also play a key role in the transport and transformation of heavy metal elements, which has a profound impact on regional and even global ecological and environmental security (Lehmann et al., 2020; Zheng et al., 2025). Global warming, in particular, creates favorable conditions for the input and mobility of heavy metals in ecosystems (Xiao et al., 2024). Soil microaggregates (<250 μm) are the core units of soil structure. They play an essential role in maintaining soil stability and regulating nutrient and carbon cycling due to their large specific surface area and surface activity. Microaggregates also significantly influence the fixation of heavy metals, mitigating ecological risks through interactions with organic matter and metal oxides (Kong et al., 2011; Totsche et al., 2018; Martens et al., 2023). In the north–south climatic transition zone of China, mountain soils are influenced by multiple coupled factors, including the temperature, precipitation, vegetation type, and parent rock, and exhibit significant vertical differentiation patterns. Elevation gradients drive non-linear changes in the soil physicochemical properties, organic matter accumulation, and heavy metal behaviour (Choudhury et al., 2016). The low temperature and high humidity at high elevations typically slow down organic matter decomposition, promote carbon pool stabilisation, and enhance heavy metal fixation (Dan et al., 2016; Sokol et al., 2022); in contrast, low-elevation regions have increased heavy metal enrichment and bioavailability due to anthropogenic activities (e.g., atmospheric deposition and industrial emissions), with a concomitant elevation of potential environmental risks (McCrackin et al., 2017; Salim et al., 2020; Witzgall et al., 2021; Duan et al., 2024).

Tongbai Mountain is located at the core of China's north–south climate transition zone. As the source of the Huaihe River and a regional ecological barrier, – it has remarkable ecological sensitivity and biodiversity (Jiang et al., 2024). The region is located in the subtropical to warm-temperate monsoon climate transition zone, and the vertical zone spectrum covers a wide range of climates, vegetation types, and soil types, providing a natural laboratory for studying elevation-driven biogeochemical processes (Liu et al., 2017). Previous studies have shown that, in mountainous areas, low-elevation regions are susceptible to exogenous pollutant deposition, while high-elevation regions exhibit significant accumulation of organic matter and weathering-resistant minerals due to low temperatures and slow weathering conditions (Choudhury et al., 2016; Tsozué et al., 2019). To date, only a handful of Chinese studies have tackled mountain soils at either the micro- or macroscopic level: Li et al. (2016) used microscopic morphology plus routine chemistry to examine organic-carbon distribution along an elevation transect in the Wuyi Mountains (Li et al., 2016), whereas Li and Guo (2022) relied on scanning-electron microscopy with energy-dispersive X-ray spectroscopy (SEM-EDS) to track aggregate-structure evolution on a karst hillslope (Li and Guo, 2022). Crucially, none of these domestic studies combined nano-scale surface spectroscopy (e.g., X-ray photoelectron spectroscopy) with bulk geochemical tools (e.g., X-ray fluorescence spectroscopy), nor did they target China's temperate–subtropical transition zone. Integrated "micro-macro" frameworks do exist elsewhere—most notably along a Peruvian Andean transect (Nottingham et al., 2018), in the Swiss Alps (Possinger et al., 2020) and in the evergreen foothills of the Ecuadorian Amazon (Bravo-Medina et al., 2023). Particularly in the special habitat of the climate transition zone, the interactions between microaggregates and heavy metals, along with their ecological effects, need to be researched in-depth (Nottingham et al., 2018; Kleber et al., 2021; Song et al., 2022). Addressing this gap is critical because mountain ecotones often act as hotspots of pollutant interception as well as climate-sensitive carbon sinks. Without a micro-scale perspective, current risk-assessment models underestimate both the downward flux of reactive metals in low-elevation soils and the long-term storage potential of organo-mineral complexes at higher elevations. Our study therefore integrates X-ray photoelectron spectroscopy (XPS), SEM-EDS mapping, X-ray fluorescence spectroscopy (XRF), Fourier transform infrared spectroscopy (FTIR) and X-ray diffraction (XRD) within a single elevation transect (200–1,140 m) to provide the first microaggregate-level evidence from China's North–South Climatic Transition Zone (Li et al.,, 2025; Totsche et al., 2018; Chen et al., 2022; Bravo-Medina et al., 2023; Li C. et al., 2024).

In direct response to the above-identified research gap, we selected Tongbai Mountain as a natural laboratory and combined XPS, SEM–EDS, XRF, FTIR and XRD to pursue three linked objectives (1) the distribution characteristics and chemical morphology of the light elements, such as C, N, and P,as well as heavy metals, such as Ti, Fe, and Mn; (2) the coupling characteristics of organic matter–mineral–heavy metals and their effects on carbon stability and heavy metal fixation; and (3) the synergistic effects of exogenous inputs and natural weathering under the elevation gradient and their ecological risk mechanisms. This study aims to reveal the biogeochemical processes of soil microaggregates in Tongbai Mountain, to provide a scientific basis for the soil management and ecological protection of mountain ecosystems in the north–south climate transition zone, and to provide theoretical support for the prediction of carbon cycling and heavy metal migration risks in the context of global change (Keller et al., 2022; Xiao et al., 2024). These findings establish a mechanistic framework for the development of elevation-adaptive soil management strategies in mountain ecosystems of China's North–South Climatic Transition Zone.

2 Materials and methods

2.1 Overview of the study area

Tongbai Mountain (112° 57′–113° 30′E, 32° 11′–32° 29′N) rises from 200 m to 1,140 m a.s.l. at the core of China's north–south climatic transition zone and forms the headwaters of the Huai River (Sun et al., 2018) (Figure 1). The massif consists mainly of Proterozoic metamorphic rocks and Yanshanian granites that

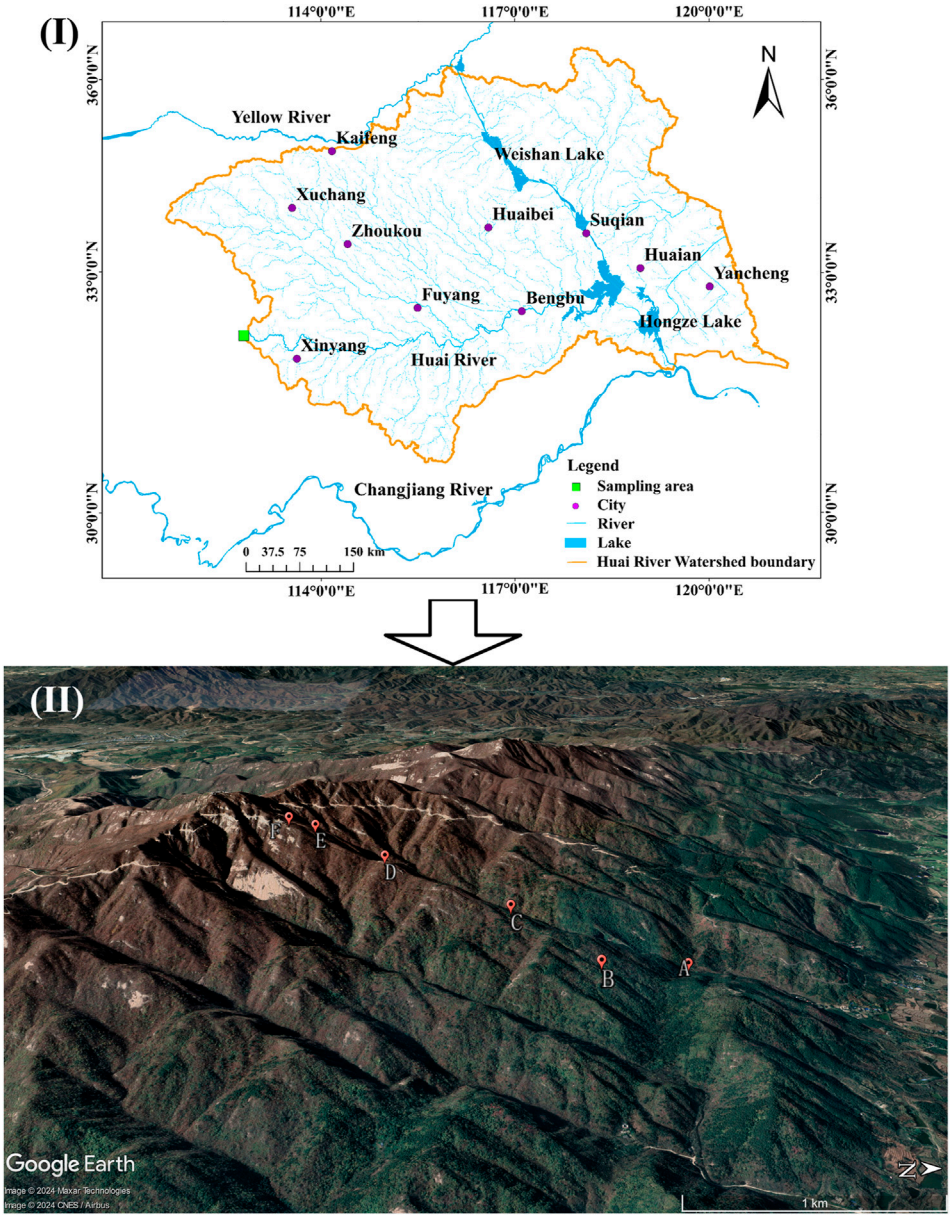

FIGURE 1
(I) Geographical map displaying the location of the study area, and (II) high-resolution satellite imagery pinpointing the spatial distribution of sampling sites (A–F).

weather into a stepped low-to mid-mountain relief with narrow V-shaped valleys and slopes commonly >25°. Soil-sampling sites A–F were positioned along the main ridge at roughly equal vertical intervals to capture this physiographic gradient (Wang et al., 2023).

2.2 Sample collection with soil microaggregate separation and extraction

In this study, an elevation gradient-based sampling strategy was used to collect 0–10 cm of topsoil from six sampling points (A–F) within the range of 200–1,140 m above sea level in Tongbai Mountain (Figure 1II). Five parallel samples were selected from each point, and about 500 g was taken after mixing for subsequent analyses. Samples were processed as follows: freezing at −80 °C for 1 h, followed by drying in a low-temperature vacuum for 24 h, and then passing through a 2 mm sieve to remove coarse particles and impurities. To separate the soil microaggregates and preserve their original structure as much as possible, the samples were mixed with a 10 mol/L $Na_4P_2O_7$ solution and ultrasonicated for 5 min; then, 0.5 mol/L NaOH solution was added at 90 °C for 30 min, centrifuged, and finally repeatedly rinsed with deionised water until neutrality was reached (Ersoy et al., 2008). Subsequently, a second extraction was carried out with 0.5 mol/L HCl solution, and the extract and washing solution were passed through an ion exchange resin to remove impurities; finally, the samples were

washed to neutrality with deionised water to obtain a relatively pure microaggregate component.

2.3 Multi-technology integration approach

We constructed a multi-scale analytical workflow (nanometre–millimetre) that couples five complementary techniques to decipher 'organic - mineral' interfaces in soil microaggregates. XPS determines surface chemical states; SEM-EDS maps micrometre-scale morphology and elemental patterns; XRF delivers bulk elemental budgets; FTIR resolves organic functional groups; and XRD identifies crystalline mineral phases. By integrating surface-sensitive (XPS), spatial (SEM-EDS), bulk (XRF), molecular (FTIR) and structural (XRD) datasets we can link nano-scale chemistry to centimetre-scale biogeochemical trends along the elevation transect. XPS is uniquely sensitive to light elements (C, N, O) and can distinguish Fe^{2+}/Fe^{3+} within the outermost 2–5 nm, but requires ultra-high vacuum and provides no spatial context. SEM-EDS achieves sub-micrometre mapping of morphology and heavy elements (Newbury et al., 2017), although matrix effects hamper quantitative C–N detection. XRF yields stable bulk concentrations (ppm-level for medium/heavy elements) over millimetre depths (Dunlea et al., 2020), yet averages redox speciation. FTIR non-destructively identifies organic functional groups, complementing mineralogical data from XRD, which in turn quantifies only crystalline phases and overlooks amorphous components. Cross-referencing these strengths allows us to triangulate heavy-metal mobility and organic–mineral interactions across the elevation gradient.

2.3.1 SED-EDS-mapping analysis of soil microaggregates

To observe the morphology and microstructure of soil microaggregates, a Zeiss GeminiSEM 360 scanning electron microscope equipped with an Xplore 30 EDS detector (Oxford, UK) probe for energy spectroscopy (Guidi et al., 2021) was used in this study. The system had an operating voltage of 5–15 kV, and the samples were treated with an ion-sputtering gold-coated film to achieve nanoscale spatial resolution and clearly present the surface morphology and pore structure of the microaggregate particles. The distribution of major elements (C, N O, P, S, Mg, Al, K, Ca, Ti, Mn, Fe) in the local area can be obtained by EDS mapping, which captures the elemental enrichment or deletion phenomena on the micrometre scale. It should be noted that this method is reliable for qualitative and semi-quantitative analyses of heavy elements, but the detection of light elements, such as C and N, is limited by the lower detection limit and matrix effects.

2.3.2 XRD analysis of mineral phases

The mineral phase analysis of microaggregates was carried out using a Rigaku SmartLab nine fully automated X-ray diffractometer (Singh and Agrawal, 2012). The test conditions were as follows: Cu-Kα target, graphite monochromator filter, tube voltage 40 kV, current 150 mA, scanning range 5°–80° (2θ), scanning speed 6° min^{-1} (2θ). Diffraction peak data were processed using Jade software and compared with standard PDF cards to determine the physical phase. Based on the adiabatic method, the content of clay minerals and non-clay minerals was calculated using the following Equation 1:

$$X_i = \left[\frac{I_i}{K_i} \Big/ \left(\sum \frac{I_i}{K_i} \right) \right] \times 100\% \quad (1)$$

where *Xi* is the percentage content of mineral i, *Ki* is the reference intensity, and *Ii* is the diffraction peak intensity.

2.3.3 XPS analysis of microaggregates

XPS analyses were performed using a Thermo Scientific Nexsa photoelectron spectrometer (Amelung et al., 2024), with a detection depth of about 2–5 nm, to obtain the chemical state information in the surface layer of microclusters. The technique offers significant advantages for the qualitative and quantitative analysis of light elements such as C and N, along with their bonding states. The instrument uses an Al-Kα excitation source (hv = 1,486.6 eV) with an operating voltage of 12.5 kV, a filament current of 16 mA, and an analytical chamber vacuum of about 8 × 10–1^0 Pa. A full-spectrum test was performed with a through energy of 100 eV, a narrow spectrum of 30 eV, and a step size of 0.1 eV, with a dwell time of 40–50 m. The data were corrected for charge using C1s = 284.80 eV. Next, baseline deduction, peak fitting, and content calculation were performed using XPSPeak 4.1 software to obtain the chemical states of the major elements and their distribution characteristics.

2.3.4 FTIR analysis of organic functional groups

FTIR was used to characterise the functional group composition and changes in soil organic matter. The samples were air-dried, passed through a 2 mm sieve, mixed with spectroscopically pure KBr at a mass ratio of 1:90, and ground and pressed (Shirshova et al., 2006; Cao et al., 2022). A Thermo Nicolet iS5 FTIR spectrometer (ThermoFisher Scientific, USA) was used, with a scanning range of 400–4,000 cm^{-1} and a resolution of 4 cm^{-1}, with 32 scans per sample being averaged. The content and distribution of functional groups were assessed by deducting the background, followed by normalising and calculating the major peak areas using the OMNIC software.

2.3.5 XRF analysis of elemental compounds

The samples were dried and ground to 200-mesh and pressed into thin sections to determine the major elements and their oxides using a wavelength-dispersive X-ray fluorescence spectrometer (AXIOS PW4400, PANalytical) (Zhang et al., 2014). Matrix effects were corrected using SuperQ 4.0 software to ensure data accuracy. This method is suitable for high-precision quantitative analysis of heavy elements such as Si, Al, Fe, Ti, Mn, Ca, and K. The test conditions were as follows: power 4.0 kW, excitation voltage 60 kV, and maximum current 125 mA.

2.4 Data statistics, modelling, and mapping

Data were analysed using SPSS 15.0 (SPSS Inc., Chicago, IL) to conduct the Pearson correlation analysis, Principal Component Analysis (PCA), and Cluster Analysis. Trend plots and heat maps were plotted in Origin 8.1 (Origin Lab Corp.). The geographic information maps of the study area and sampling sites were generated using ArcGIS 10.0 (ESRI, Redlands, CA, USA). Satellite

TABLE 1 Elemental composition of samples A to F determined by XPS (Wt. %).

Element	A	B	C	D	E	F
C	22.96	21.12	22.99	27.86	23.70	23.33
N	1.79	2.05	1.89	2.19	2.37	2.13
O	52.87	54.40	53.10	49.47	52.50	51.39
Al	13.50	14.59	14.10	13.31	13.06	13.05
P	1.03	0.95	1.05	1.04	0.94	1.43
Ca	1.79	1.35	1.24	1.25	1.17	1.37
Ti	1.07	1.06	1.04	0.95	0.90	1.15
Mn	1.61	1.12	0.87	1.13	1.00	1.19
Fe	3.37	3.36	3.72	2.81	4.35	4.93

images for Figure 1II were obtained from Google Earth Pro 7.3.6.9796.

3 Experimental results

3.1 Elevation gradient patterns of soil microaggregate elements determined through multiscale coupling

XPS shows that Ti in the microaggregate surface layer (≈1–10 nm) is low and uniform, ranging from 0.90% to 1.15% across all sites (Table 1; Figure 2). Such values imply only trace amounts of weathering-resistant Ti minerals, notably rutile, on aggregate surfaces. By contrast, SEM–EDS maps reveal little Ti inside the aggregates; in several samples it is undetectable. The element therefore occurs only in very localised interior domains (Figures 2, 3). Bulk XRF measurements confirmed that total Ti content in these soils was low (0.24%–0.41% by weight, Table 3), with a slight increase up to 0.41% at the highest site (F) (Figure 2). Ti is usually in the form of oxide minerals and often coexists with Fe (Lyu et al., 2017). This pattern reflects Ti's behavior as a stable element largely confined to resistant mineral phases in the deep soil (Tables 1–3; Figures 2–5).

XPS results showed that Mn in the microaggregate surface layer reached as high as 1.61% at the lowest elevation site A (Table 1). This suggests that Mn oxides or reduced Mn compounds are present in the surface microaggregates at low elevation. However, SEM-EDS detected only about 0.1% Mn at site A and none at the other sites, indicating that Mn is not present in appreciable amounts in the interior of the microaggregates. XRF analysis further showed that overall Mn levels were extremely low (0.02%–0.05% total) and sparsely distributed across all samples (Table 3). The pronounced enrichment of Mn in the surface microaggregates at site A appears to be closely related to specific environmental conditions at low elevation.

SEM-EDS data for Fe showed a highly heterogeneous distribution at the micrometer scale: in deeper microaggregate regions, Fe ranged from a high of 4.6% at site B (low elevation) to as low as 0.5% at site F (high elevation) (Table 2; Figure 4).

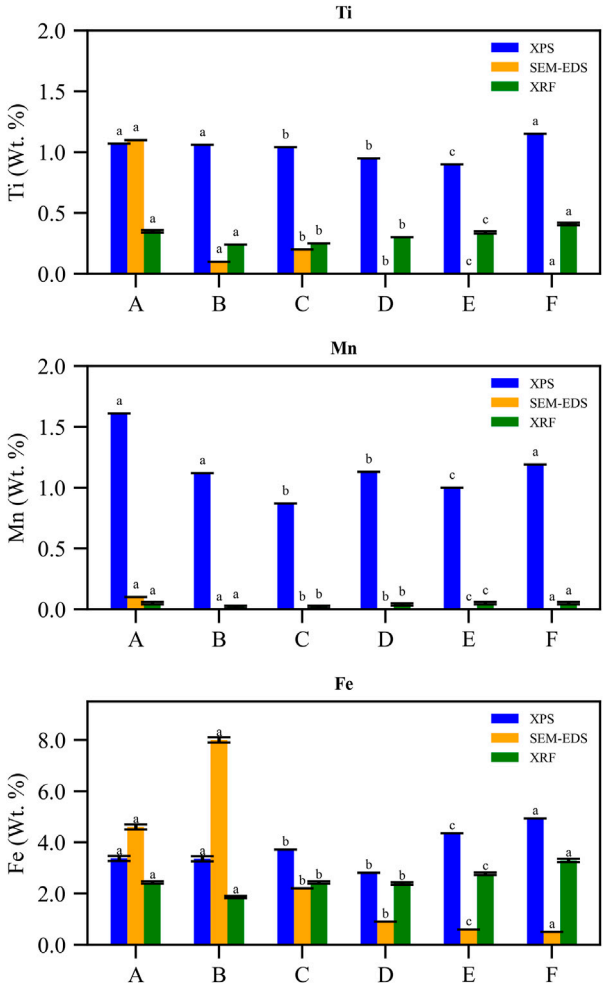

FIGURE 2
Comparative analysis of Ti, Mn, and Fe contents using XPS, SEM-EDS, and XRF across sampling locations A to F; error bars indicate ±SE. Different lowercase letters above bars denote significant differences among sites (Tukey's HSD, α = 0.05): *a* ($p < 0.01$), *b* ($p < 0.05$), *c* ($p < 0.10$).

Meanwhile, XRF measurements indicated that the bulk Fe content of the soil increased steadily with elevation, from 1.86% at site B up to 3.29% at site F (Table 3). Thus, although total Fe is higher at the summit, Fe within microaggregates is unevenly distributed—enriched in some zones but not uniformly so. Notably, Fe appears enriched in both surface and deep microaggregate layers at certain mid-elevation sites, reflecting significant spatial heterogeneity (Figure 2).

XPS measurements further showed that C comprised about 22.96%–27.86% of the surface layer of microaggregates across the sites (Table 1). N was slightly higher in the surface of the high-elevation samples E and F (2.19%–2.37%) compared to others, and P ranged from 0.94% to 1.43%. These values suggest that a substantial amount of organic matter is present in the microaggregate surfaces, particularly at the higher elevations. O content in the surface layer was 49.47%–54.40% by XPS, whereas SEM-EDS showed O in the range of 38.9%–49.3% for microaggregate interiors (Table 2). Al in the surface layer remained relatively constant according to XPS (13.05%–14.59%), but SEM-EDS detected a pronounced change in

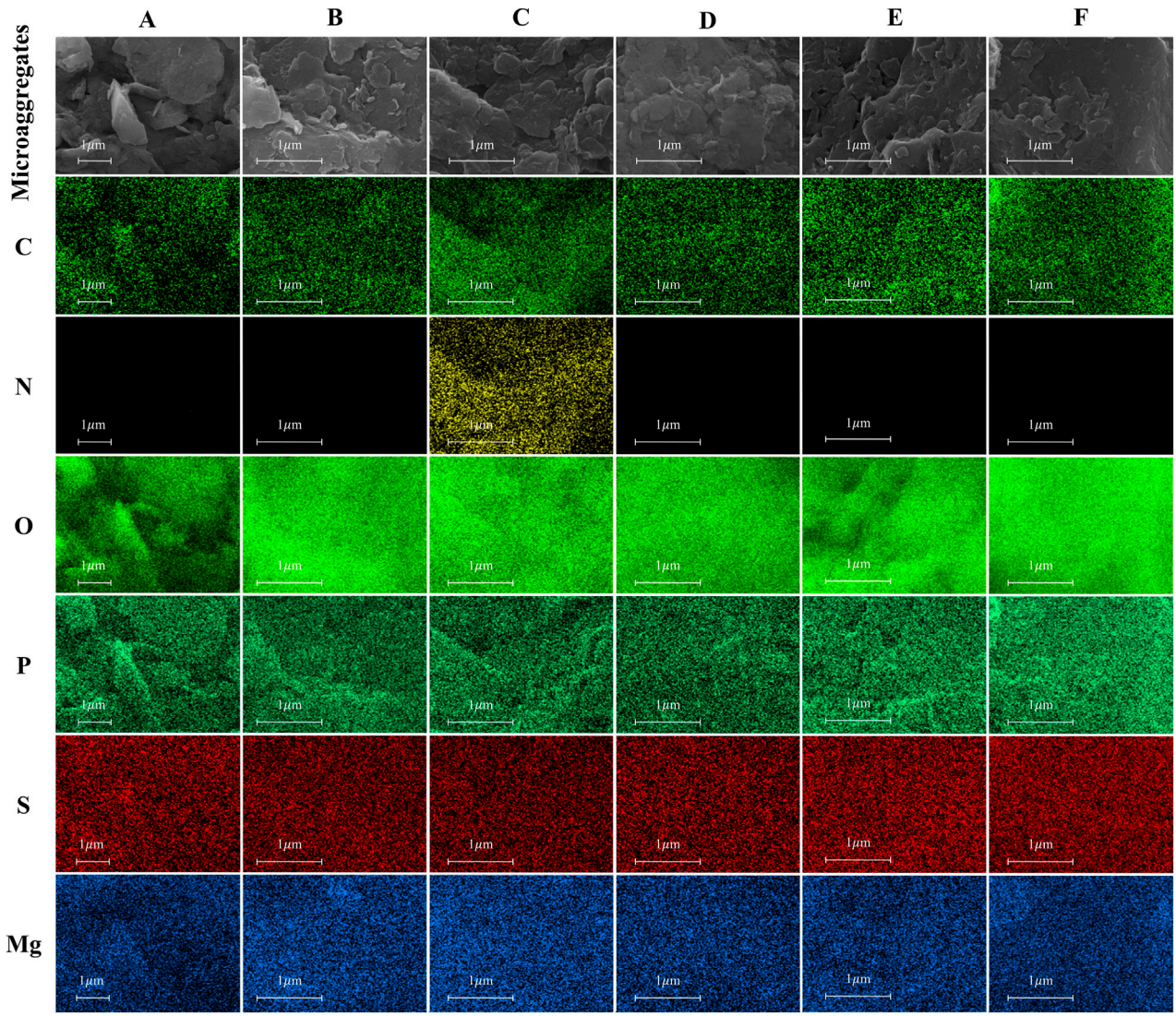

FIGURE 3
SEM-EDS elemental mapping of microaggregates **(A-F)** showing distributions of C, N, O, P, S, and Mg.

Al with elevation: up to 14.9% in deeper microaggregate portions at low-elevation site A, dropping to ~1.0% at high-elevation site F (Table 2). Ca in the surface layer was 1.17%–1.79% (XPS), and SEM-EDS found only a localized Ca presence (about 1.6% at site E), indicating that Ca distribution is patchy and does not follow a clear elevation trend. The surface enrichment of Mn at low elevations (XPS Mn = 1.61% at site A vs only ~0.1% in the interior and 0.02%–0.05% total by XRF) highlights the influence of a reducing environment in concentrating Mn in surface coatings at those sites. Fe showed an uneven profile: XPS recorded 4.93% Fe at the high elevation site F (in the surface layer) and similarly elevated Fe at mid-elevation, while SEM-EDS revealed hotspots (8.0% Fe at site B interior) and depletions (0.5% at site F interior), underscoring high Fe mobility and redistribution. Meanwhile, the accumulations of C and N at the upper elevation sites (with XPS measuring up to 4.93% Fe and 1.15% Ti at site F) suggest that stable organo-mineral complexes (often involving Fe and Ti oxides) become more prevalent toward the summit.

3.2 Elevation-driven mechanisms for the evolution of the chemical forms of key elements

In this study, we investigated how the chemical forms of key elements—particularly carbon (C), nitrogen (N), phosphorus (P), and iron (Fe)—evolve with elevation using XPS high-resolution spectral analysis (Figure 6). XPS peak fitting revealed clear elevation trends in organic functional groups: the fraction of carbon present as carbon–carbon bonds (C–C/C=C, representing relatively unoxidized carbon skeletons) slightly decreased from 54.5% at the low-elevation site A to 46.8% at the high-elevation site F (Figures 7, 8; Table 4). Conversely, the fraction of carbon bound to nitrogen (C–N) increased appreciably, from 19.2% at site A to 26.4% at site F (Table 4). The proportions of C–O and COOH (carboxyl) functional groups showed much smaller variation, remaining around 13.8%–15.9% for C–O and 10.9%–13.9% for COOH across the gradient. Notably, the COOH content was

TABLE 2 Elemental composition of samples A to F determined by SEM-EDS (Wt. %).

Element	A	B	C	D	E	F
C	10.8 ± 0.6	7.7 ± 0.4	24.4 ± 0.4	10.0 ± 0.4	6.2 ± 0.4	10.2 ± 0.4
N	0.0 ± 0.5	0.0 ± 0.4	1.8 ± 0.5	0.0 ± 0.0	0.0 ± 0.0	0.0 ± 0.3
O	38.9 ± 0.3	47.0 ± 0.2	39.6 ± 0.3	46.8 ± 0.2	45.2 ± 0.2	49.3 ± 0.2
Na	0.2 ± 0.0	N/A	1.5 ± 0.0	1.2 ± 0.0	5.8 ± 0.0	0.2 ± 0.0
Mg	0.9 ± 0.0	N/A	0.5 ± 0.0	0.2 ± 0.0	0.1 ± 0.0	0.1 ± 0.0
Al	14.9 ± 0.1	11.0 ± 0.1	10.5 ± 0.1	12.9 ± 0.1	12.0 ± 0.1	1.0 ± 0.0
Si	24.2 ± 0.2	21.7 ± 0.1	17.8 ± 0.1	23.0 ± 0.1	27.7 ± 0.1	38.2 ± 0.2
P	0.6 ± 0.0	0.4 ± 0.0	0.2 ± 0.0	0.1 ± 0.0	0.2 ± 0.0	0.1 ± 0.0
S	0.4 ± 0.0	0.2 ± 0.0	0.2 ± 0.0	0.1 ± 0.0	0.1 ± 0.0	0.1 ± 0.0
K	2.1 ± 0.1	3.6 ± 0.0	1.1 ± 0.0	4.7 ± 0.0	0.3 ± 0.0	0.1 ± 0.0
Ca	1.0 ± 0.0	0.2 ± 0.0	0.1 ± 0.0	0.1 ± 0.0	1.6 ± 0.0	N/A
Ti	1.1 ± 0.0	0.1 ± 0.0	0.2 ± 0.0	N/A	N/A	N/A
Mn	0.1 ± 0.0	N/A	N/A	N/A	N/A	N/A
Fe	4.6 ± 0.1	8.0 ± 0.1	2.2 ± 0.0	0.9 ± 0.0	0.6 ± 0.0	0.5 ± 0.0

TABLE 3 Elemental composition of samples A to F determined by XRF (Wt. %).

Element	A	B	C	D	E	F
Ti	0.35 ± 0.01	0.24 ± 0.00	0.25 ± 0.00	0.30 ± 0.00	0.34 ± 0.01	0.41 ± 0.01
V	0.00 ± 0.00	0.00 ± 0.00	0.00 ± 0.00	0.00 ± 0.00	0.00 ± 0.00	0.00 ± 0.00
Mn	0.05 ± 0.01	0.02 ± 0.01	0.02 ± 0.01	0.04 ± 0.01	0.05 ± 0.01	0.05 ± 0.01
Fe	2.43 ± 0.05	1.86 ± 0.04	2.43 ± 0.05	2.39 ± 0.05	2.77 ± 0.05	3.29 ± 0.06
Cu	0.00 ± 0.00	0.00 ± 0.00	0.00 ± 0.00	0.00 ± 0.00	0.00 ± 0.00	0.00 ± 0.00
Zn	0.01 ± 0.00	0.01 ± 0.00	0.01 ± 0.00	0.01 ± 0.00	0.01 ± 0.00	0.02 ± 0.00
Rb	0.01 ± 0.00	0.01 ± 0.00	0.01 ± 0.00	0.02 ± 0.00	0.01 ± 0.00	0.01 ± 0.00
Sr	0.02 ± 0.00	0.07 ± 0.00	0.04 ± 0.00	0.04 ± 0.00	0.04 ± 0.00	0.02 ± 0.00
Y	0.01 ± 0.00	0.01 ± 0.00	0.00 ± 0.00	0.00 ± 0.00	0.01 ± 0.00	0.01 ± 0.00
Zr	0.07 ± 0.00	0.08 ± 0.00	0.04 ± 0.00	0.04 ± 0.00	0.05 ± 0.00	0.04 ± 0.00
Ba	0.04 ± 0.04	0.08 ± 0.04	0.06 ± 0.04	0.06 ± 0.04	0.06 ± 0.04	0.00 ± 0.00
Pb	0.01 ± 0.00	0.01 ± 0.00	0.01 ± 0.00	0.01 ± 0.00	0.01 ± 0.00	0.01 ± 0.00

slightly higher at the low-elevation sites A and B, whereas nitrogen-containing and other unsaturated bonding groups became more abundant in the high-elevation samples (sites E and F). The XPS N 1s spectra also revealed an elevational shift in nitrogen forms: the proportion of Pyridinic-N (aromatic, ring-bound N) increased from 21.1% at site A to 44.4% at site F (Figures 7, 9; Table 4). In contrast, Pyrrolic-N decreased from 42.9% to 25.2%, and Quaternary-N (alkylated N) declined from 24.1% to 19.6% between sites A and F. The oxidized nitrogen species showed little overall change with elevation, aside from a slight peak (~17.1%) at the mid-elevation site D. Phosphorus showed significant variability: total P (by XPS) ranged from 0.38% at site B (lowest) to 1.06% at site D (highest), with other sites between ~0.5% and 1.02%. XPS analysis of the P 2p region indicated that P in all samples exists predominantly as inorganic phosphate, with only minor contributions from organic P compounds (Figure 10; Table 4). Mid-elevation site D, which had the highest P content, stands out as a zone of enhanced P accumulation, whereas the low-elevation site B had the least P. In summary, elevation strongly influences the chemical bonding states of C, N, P, and Fe in soil microaggregates.

The ratio of ferrous to ferric iron (Fe^{2+}/Fe^{3+}) also varied systematically with elevation (Figure 11; Table 4). At the low-elevation sites A and B, a substantial portion of total Fe was present as Fe^{2+} (reduced iron). At mid-elevations (sites C and D), the proportion of Fe present as Fe^{3+} increased sharply–for example, Fe^{3+} constituted about 62.4% of total Fe at site C and 55.7% at site D.

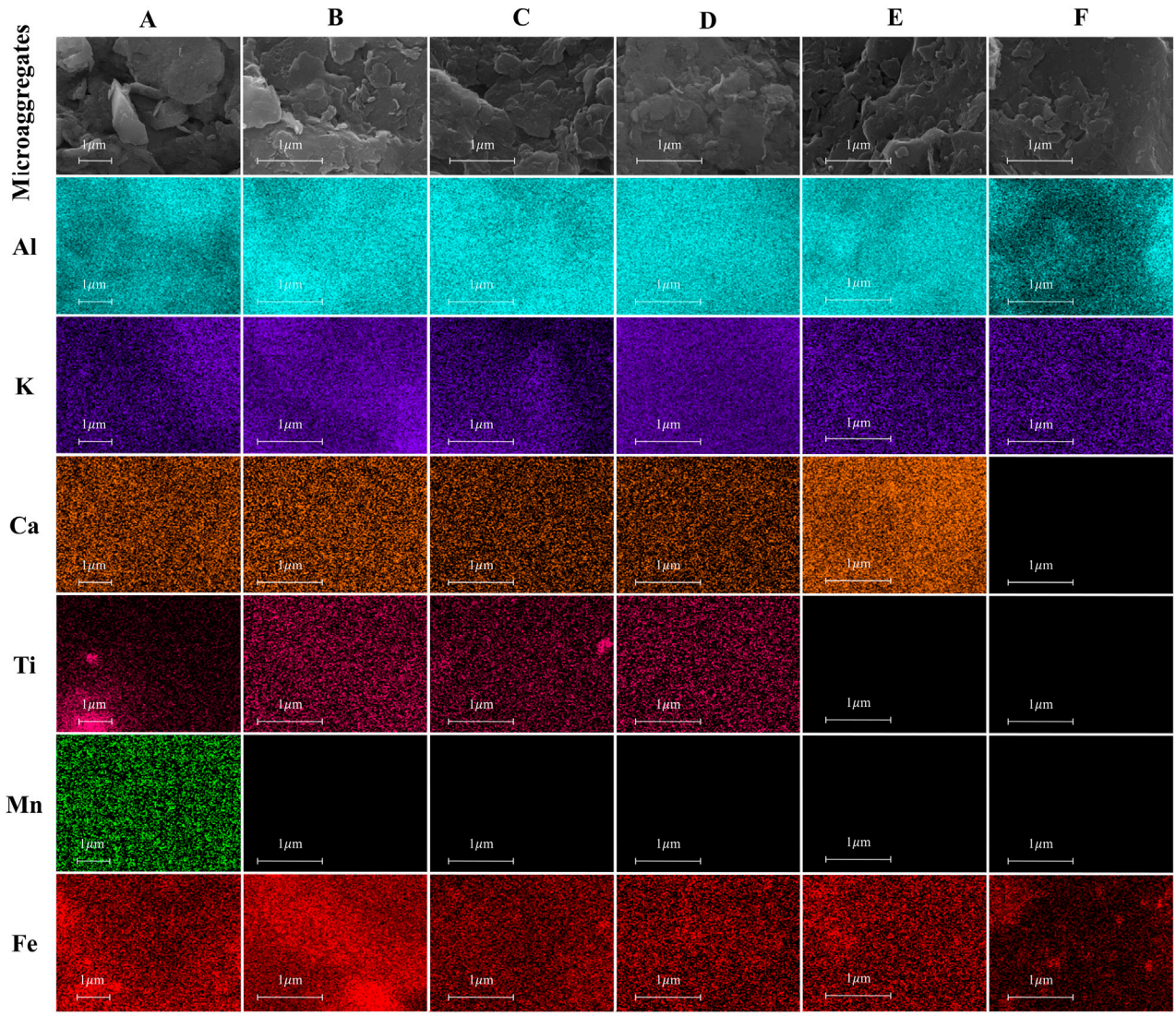

FIGURE 4
SEM-EDS characterization of microaggregates **(A-F)** revealing elemental distributions of Al, K, Ca, Ti, Mn, and Fe.

At the high-elevation sites E and F, Fe^{3+} remained the dominant form of iron, although there was a minor relative increase in Fe^{2+} at site E compared to the mid-elevation sites. Overall, elevation had a strong effect on iron redox state: low-elevation microaggregates contained more Fe in the reduced form, whereas Fe in the mid- and high-elevation microaggregates was predominantly in the oxidized form (Fe^{3+}). This clear shift from Fe^{2+} to Fe^{3+} with increasing elevation reflects more oxidizing soil conditions at higher elevations.

3.3 Changes in microaggregate structure, mineral composition, and organic functional groups with elevation and their interactions

SEM imaging revealed a pronounced change in microaggregate structure with elevation in Tongbai Mountain. At the low-elevation sites (A and B), soil microaggregates were composed of irregularly shaped particles with rough surfaces and abundant pore space, resulting in a loose, porous aggregate structure (Figures 3, 4). In contrast, at the high-elevation sites (E and F), microaggregates had a much more compact structure: the particles were tightly bound together and porosity was greatly reduced. These structural differences clearly illustrate the influence of elevation on the physical architecture of the soil—low-elevation conditions produce more open, fragmented microaggregates, whereas high-elevation conditions foster tightly aggregated soil structure.

XRD analysis showed systematic variations in mineral composition along the elevation gradient. The content of microcline (a potassium feldspar) peaked at 29.7% at the mid-elevation site C, then declined sharply to about 5.5% at the high-elevation site F (Figure 12). Similarly, albite (a plagioclase feldspar) reached its highest content (34.0%) at the relatively low elevation site B and then decreased progressively with further elevation gain. In contrast, the content of clay minerals such as kaolinite and chlorite varied only slightly with elevation, showing minor fluctuations but no strong trend (Xu Y. et al., 2022). These results suggest that easily weatherable minerals like feldspars are most abundant at middle

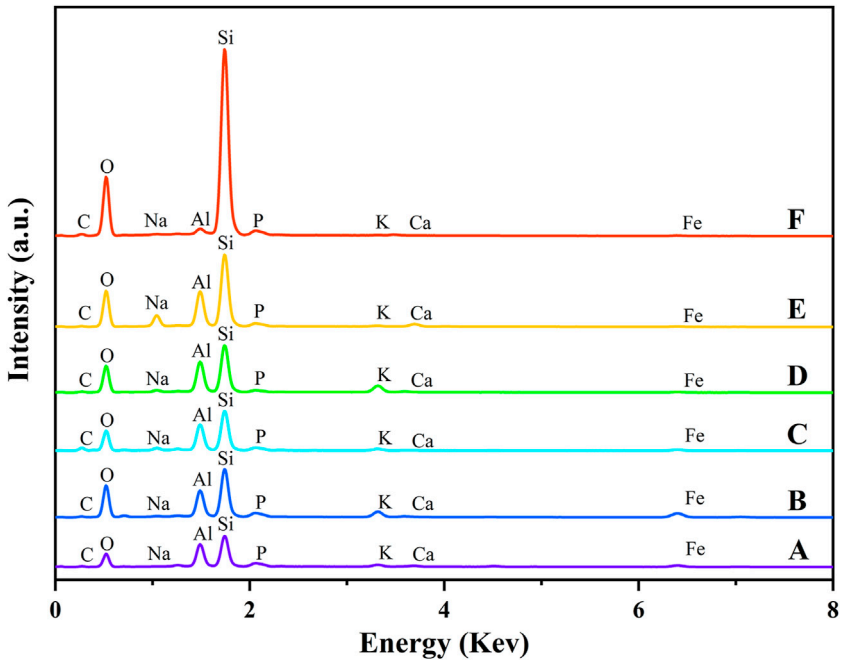

FIGURE 5
EDS spectra of samples across sampling locations A to F.

elevations and become less prevalent at the highest, most weathered sites, whereas resilient clay minerals are present in comparable proportions throughout the gradient.

FTIR analysis further revealed elevation-driven differences in soil organic matter functional groups. In the high-elevation soils, the absorbance peaks at 3,423 cm^{-1} (O–H and N–H stretching vibrations) and 2,929 cm^{-1} (aliphatic C–H stretches) were significantly more intense–at site F, the relative peak areas reached about 49.97% for the 3,423 cm^{-1} band and 5.88% for the 2,929 cm^{-1} band (Figures 13, 14). This indicates a greater abundance of hydroxyl, amine, and aliphatic functional groups in the soil organic matter at high elevation (Figure 13) (Tang et al., 2023). Additionally, the absorption peak at 1,631 cm^{-1} (attributable to aromatic C=C and/or conjugated C=O groups) was strongest at high elevation (with a maximum intensity of 15.23% at site F), reflecting an enrichment of aromatic compounds in the organic matter of those soils (Cao et al., 2022). In summary, as elevation increases, there is a notable increase in hydrophilic (polar) and aliphatic organic functional groups, as well as aromatic structures, within the soil microaggregates. This pattern likely stems from the cooler, wetter high-elevation environment, which promotes the retention of certain organic compounds (e.g., phenolic and aliphatic components) and active nitrogen cycling, leading to more complex and humified soil organic matter at the mountain summit.

4 Discussion

4.1 Distribution characteristics and chemical morphology

Elemental and chemical patterns across the elevation gradient reflect a coordinated interplay between organic inputs, mineral transformations, and redox processes. The pronounced enrichment of surface carbon at mid to high elevations likely results from dense vegetation cover and reduced decomposition rates under cooler, wetter conditions, which favor the accumulation of organic residues and their stabilization on mineral surfaces. These findings are consistent with previous reports highlighting the role of vegetation density and climate in shaping soil carbon profiles across montane landscapes (Calderón et al., 2013; Witzgall et al., 2021; Wasner et al., 2024).

XPS high-resolution spectra indicate a progressive transformation in organic matter chemistry with elevation. The decline in unsubstituted carbon structures (C–C/C=C) alongside an increase in nitrogen-containing groups (C–N) suggests enhanced molecular complexity and greater functionalization of soil organic matter at higher elevations (Yin et al., 2022). This transformation is further supported by surface oxygen enrichment, attributed to elevated levels of oxygenated organic groups and metal oxides, which points to more reactive and hydrophilic organic matter in highland soils (Lehmann and Kleber, 2015; Li C. et al., 2023).

Changes in iron redox speciation further underscore the influence of elevation on soil geochemistry. The dominance of Fe^{2+} in lowland sites reflects reducing conditions that inhibit iron oxidation, whereas mid-elevation zones exhibit a clear shift toward Fe^{3+} dominance, indicative of more oxidizing environments. Interestingly, a partial reversion toward Fe^{2+} at the summit suggests localized reduction effects, potentially driven by concentrated organic matter inputs and limited oxygen diffusion (Shaheen et al., 2019; Duiker et al., 2003; Duiker et al., 2003). They also suggest varying degrees of parent-material weathering and mineral transformation along the elevation gradient, as observed in other mountainous soils (Barber et al., 1992; Liu et al., 2017).

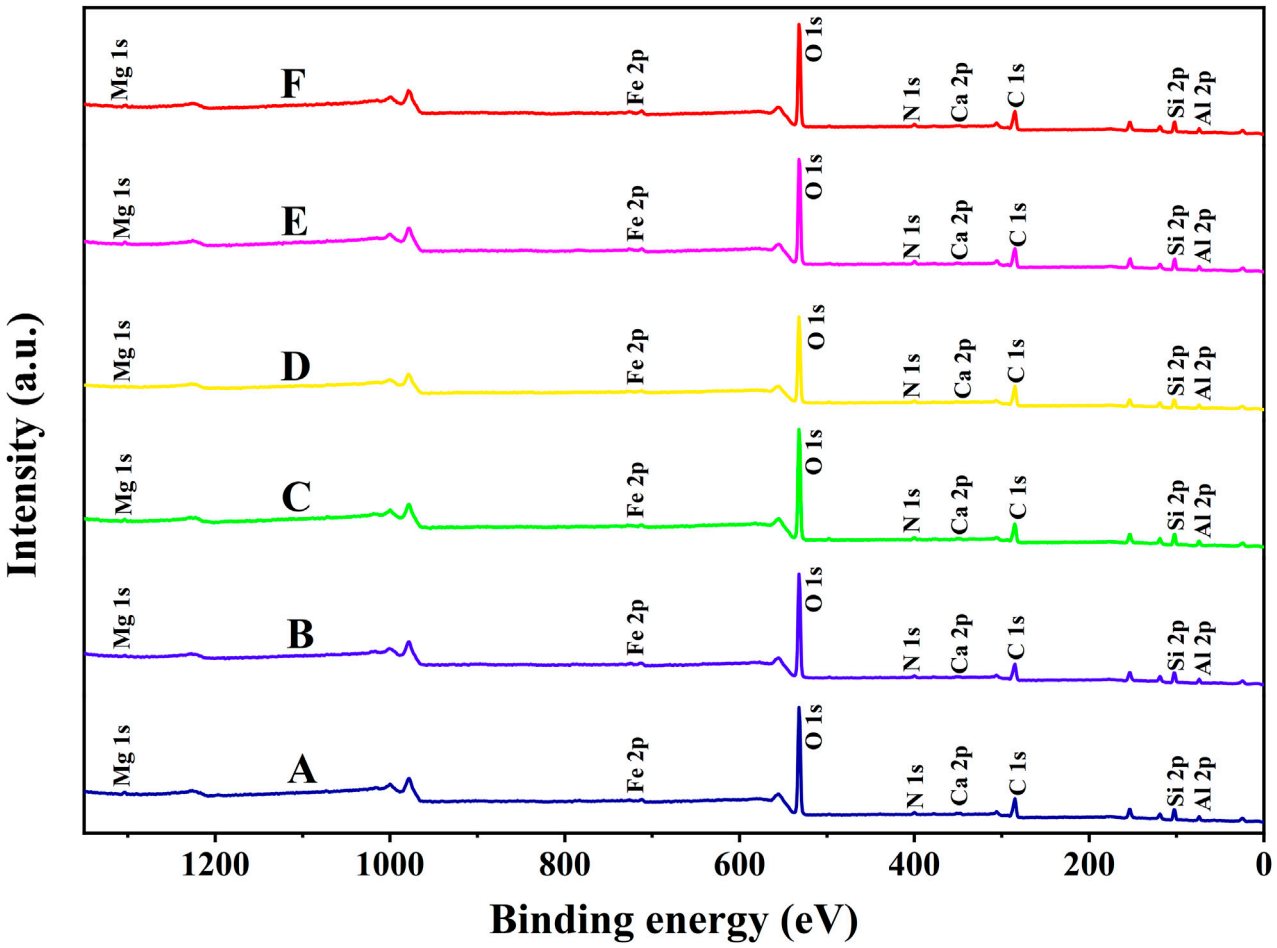

FIGURE 6
XPS survey spectra across sampling locations A to F.

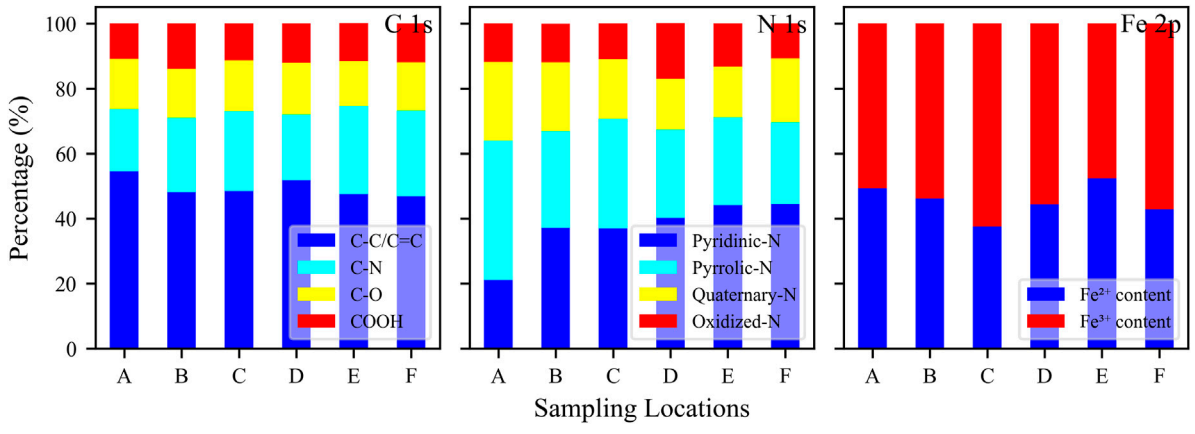

FIGURE 7
Elemental composition analysis by XPS for C 1s, N 1s, and Fe 2p across sampling locations A to F.

Nitrogen and phosphorus also exhibit marked surface enrichment at higher elevations, pointing to enhanced nutrient retention in organically complexed forms. These patterns reinforce the role of stable particulate organic matter in sequestering essential elements near the soil surface (Witzgall et al., 2021; Jindo et al., 2023). The phosphorus distribution, in particular, suggests that mineral–organic interactions at higher elevations facilitate surface accumulation while limiting

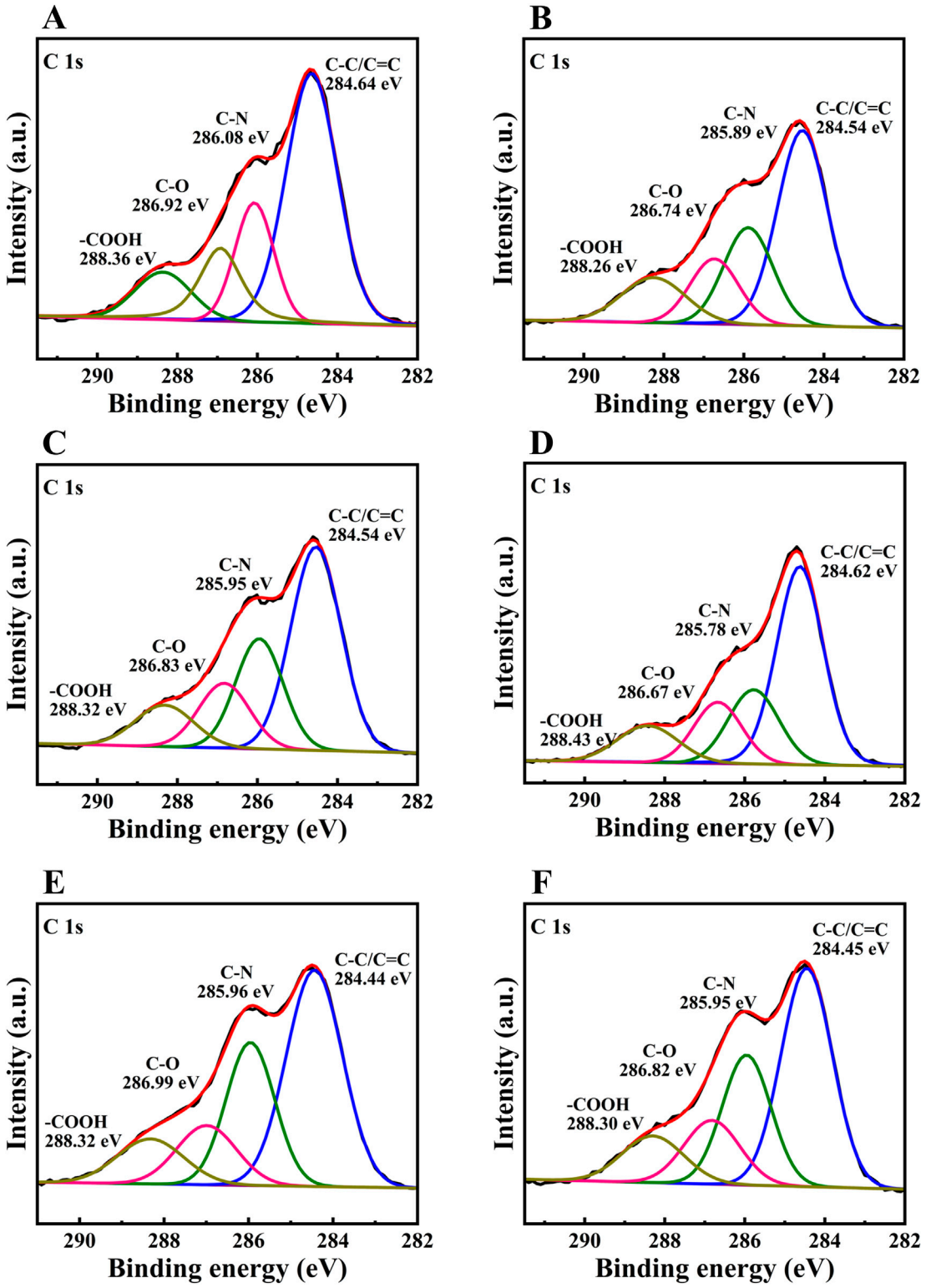

FIGURE 8
High-resolution XPS C 1s spectra of samples across locations **(A–F)**.

subsurface migration. Inorganic elements further reflect distinct geochemical regimes. Surface titanium levels remained low but showed a slight increase with elevation, consistent with the accumulation of resistant Ti-bearing phases following prolonged weathering (Wang et al., 2022; Solymos et al., 2024). Manganese enrichment at low elevations highlights the strong influence of reducing environments on its mobility and surface retention (Chacon et al., 2018). In contrast, calcium exhibited no

TABLE 4 XPS quantitative analysis of chemical states across sampling locations A to F.

Chemical states	A	B	C	D	E	F
C-C/C=C	54.50%	48.10%	48.40%	51.80%	47.50%	46.80%
C-N	19.20%	22.80%	24.60%	20.20%	27.10%	26.40%
C-O	15.40%	15.20%	15.60%	15.90%	13.80%	14.80%
COOH	10.90%	13.90%	11.40%	12.10%	11.70%	12.00%
Pyridinic-N	21.10%	37.20%	37.00%	40.20%	44.10%	44.40%
Pyrrolic-N	42.90%	29.60%	33.70%	27.10%	27.00%	25.20%
Quaternary-N	24.10%	21.20%	18.30%	15.70%	15.70%	19.60%
Oxidized-N	11.90%	11.90%	11.00%	17.10%	13.20%	10.80%
P	1.02%	0.38%	0.51%	1.06%	0.60%	0.97%
Fe^{2+}	49.30%	46.10%	37.60%	44.30%	52.40%	42.80%
Fe^{3+}	50.70%	53.90%	62.40%	55.70%	47.60%	57.20%

consistent elevational trend, reflecting its heterogeneous inputs and site-specific redistribution (Igwe et al., 2005).

Importantly, the correlation analysis (Figure 15) revealed that the positive correlation between carbon and iron strengthened at higher elevations (especially at site F). This suggests enhanced formation of stable organo–iron complexes under cold, humid conditions at the summit. Such organo-mineral associations are known to promote carbon retention in soils (Lehmann and Kleber, 2015), as also demonstrated experimentally by Zhao et al. (2023) and Li X. et al. (2024). Multivariate analyses of our data (PCA and clustering; Figure 16) grouped the microaggregate samples into three broad categories corresponding to low-, mid-, and high-elevation regimes. Sites A (lowest) and F (highest) each formed distinct end-members in multivariate space, while the mid-elevation sites B, C, D, and E clustered together. This pattern indicates that the altitudinal gradient imposes a systematic modulation on microaggregate properties. Similarly, Wu et al. (2021) found that soil characteristics in mountainous terrain tend to cluster by elevation, reflecting the integrated influence of elevation-related factors. In summary, increasing elevation drives a multi-scale differentiation of elemental distributions and soil characteristics—from the microaggregate surface chemistry to bulk soil composition—mediated by changes in temperature, moisture, vegetation, and weathering processes (He et al., 2016; Li et al., 2016).

4.2 Coupling characteristics of organic matter–mineral–heavy metals

Fourier-transform infrared (FTIR) spectra showed clear elevation effects on the soil organic matter functional groups. The absorption peaks at 3,423 cm^{-1} (O–H/N–H stretching) and 2,929 cm^{-1} (aliphatic–CH_2 stretching) were markedly enhanced in the high-elevation samples (sites E and F) (Figure 13). These stronger peaks indicate that polar functional groups (such as hydroxyls and amines) and aliphatic structures are significantly more abundant at higher elevations. This trend is in agreement with Cao et al. (2022), who found that high-elevation soils tend to have a greater abundance of–OH and–CH functional groups due to cooler, wetter conditions. In addition, the absorption band at 1,631 cm^{-1} (aromatic C=C and conjugated C=O) was intensified at the mid- and high-elevation sites (particularly D and F). This reflects higher aromaticity and a greater degree of humification in the soil organic matter at these elevations (Tsozué et al., 2019; Kleber et al., 2021).

Consistent with the FTIR observations, XPS C 1s analyses confirmed the formation of more oxidized and nitrogen-rich organic structures as elevation increased. High-resolution XPS data revealed a decrease in unsubstituted carbon structures and an increase in C–N bonds with elevation, indicating greater enrichment of nitrogenous organic compounds and more advanced humification at higher elevations (Wang et al., 2016). Under the high-temperature and high-humidity conditions at low elevations, strong microbial activities and significant leaching, and frequent redox fluctuations, iron oxides became susceptible to mineral phase transformation, which in turn released and decomposed the organic carbon bound to them (Chen et al., 2020). Choudhury et al. (2016) reported a similar trend of increasing organic N content with elevation, supporting the idea that cooler high-elevation environments promote the accumulation of N-rich, humified organic matter. XPS N 1s spectra revealed a shift toward more stable aromatic nitrogen forms at higher elevations, suggesting enhanced preservation of organic matter through binding with iron oxides and clay minerals (Chen et al., 2018; Li Q. et al., 2023).

The content of clay minerals–such as Kaolinite and Chlorite–varied less, exhibiting only slight fluctuations (Xu Y. et al., 2022). Xiao et al. (2023) proposed the soil mineral carbon pump (MnCP), in which clays and Fe/Mn oxides actively convert labile organic matter into long-lived mineral-associated carbon via adsorption, aggregation, and redox-catalyzed polymerization (Xiao et al., 2023). The pyridinic-N enrichment and Fe^{3+}-dominated organo-mineral complexes we observed above 700 m closely mirror the deterministically assembled specialist microbial

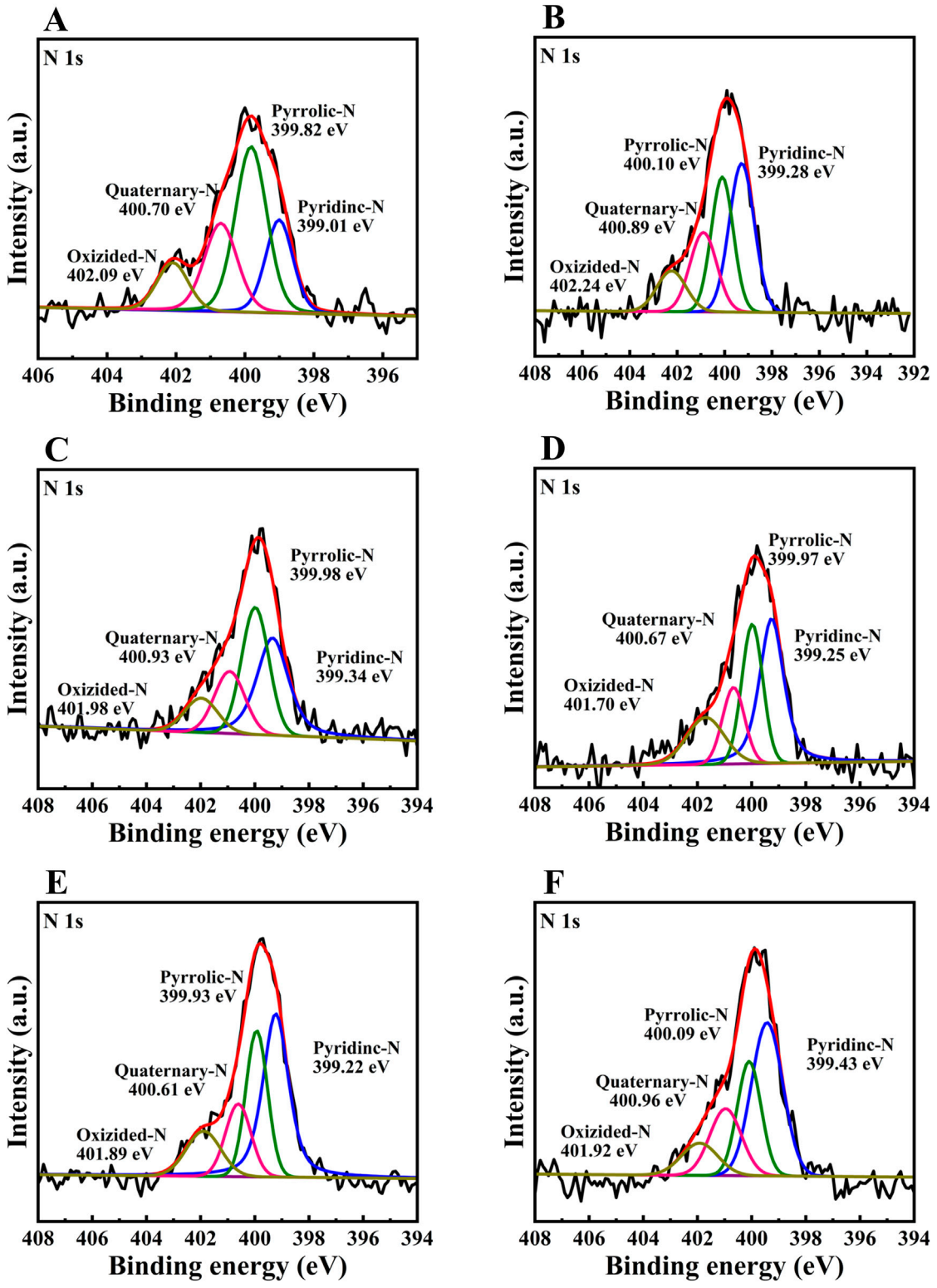

FIGURE 9
High-resolution XPS N 1s spectra of samples across locations **(A–F)**.

communities documented by Yang et al. (2025) near the Tibetan timberline, suggesting that these niche-adapted taxa may catalyse and sustain the stable C–N–Fe linkages identified in our soils (Yang et al., 2025). The correlation matrix quantitatively corroborates that the O–H/N–H band is strongly and positively associated with illite, chlorite and quartz (Figure 15). Oxidised carbon (C–O/COOH) shows a positive correlation with Fe^{3+}, whereas unsubstituted C–C/C=C is inversely related. Chlorite, in turn, couples significantly with

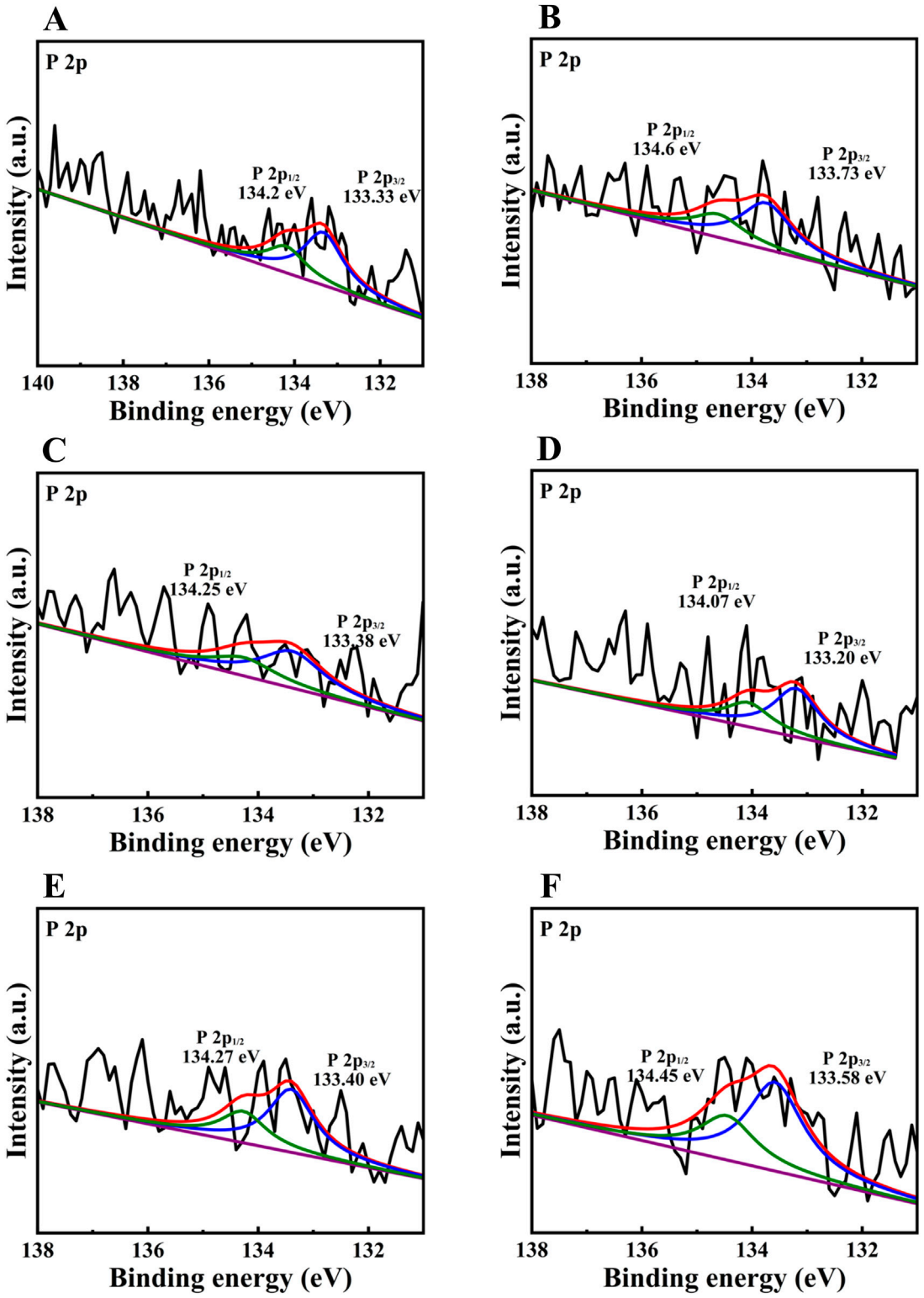

FIGURE 10
High-resolution XPS P 2p spectra of samples across locations **(A–F)**.

both pyridinic-N and the aromatic C=C/C=O band, highlighting the preferential sequestration of N-rich aromatic moieties at specific clay sites (Ivashchenko et al., 2021). Overall, the coupling between organic matter and mineral phases strengthens with elevation—high-elevation soils show more evidence of complex organo-mineral interactions (through functional groups and metal coordination), which in turn enhance carbon persistence and heavy-metal retention in the microaggregates.

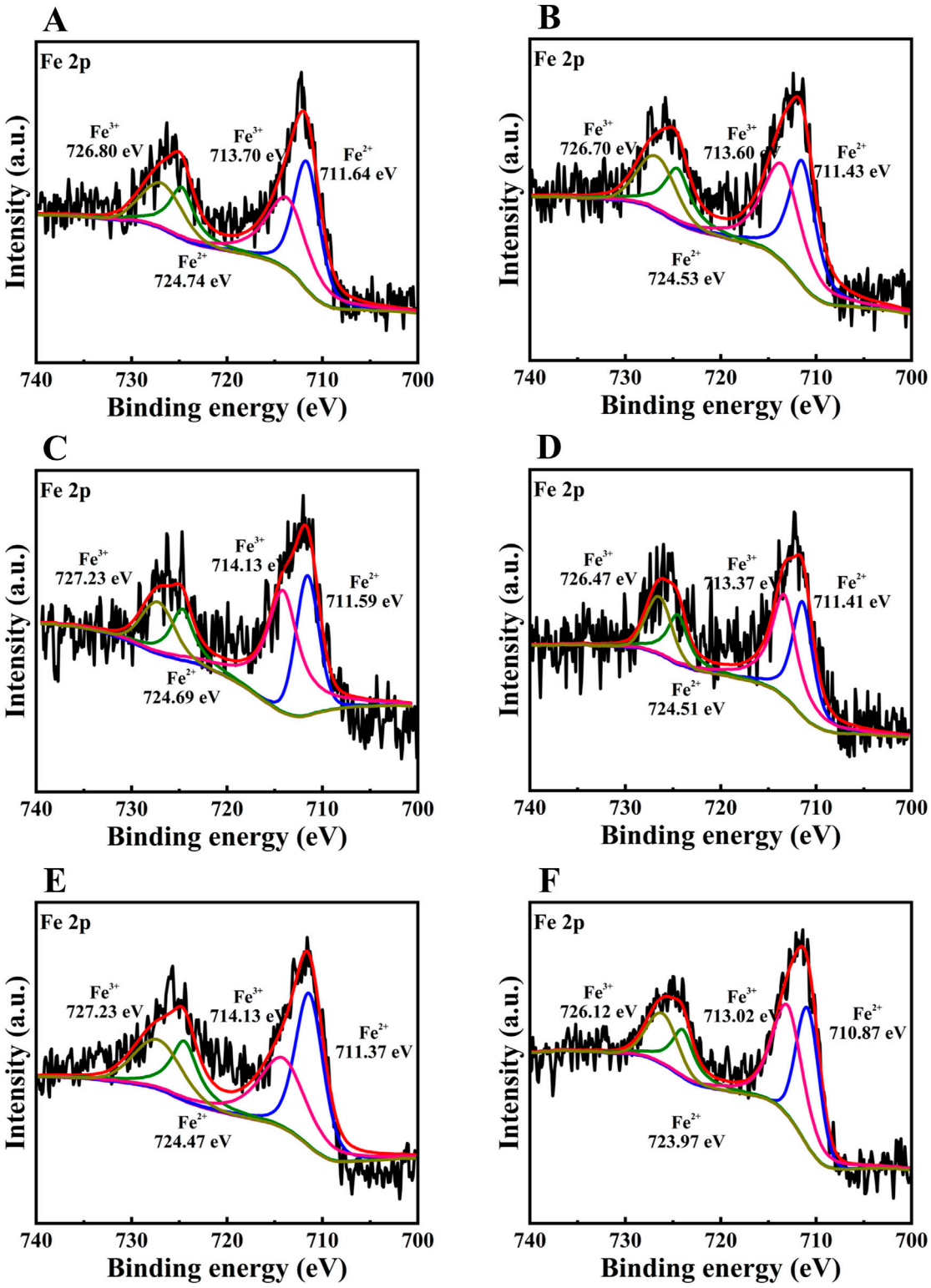

FIGURE 11
High-resolution XPS Fe 2p spectra of samples across locations **(A–F)**.

4.3 Synergistic effects of exogenous inputs and natural weathering

Hierarchical clustering of the six sampling sites (A–F), based on FTIR, XPS, and mineralogical data, revealed three distinct elevation-dependent groups (Figure 16). Low-elevation sites (A and B) were enriched in aliphatic ($-CH_2$) and unsubstituted carbon (C–C/C=C), with fewer nitrogenous or oxidized compounds and weaker mineral associations—indicating more reactive, less stabilized organic matter. Mid-elevation sites (C and D) exhibited mixed features,

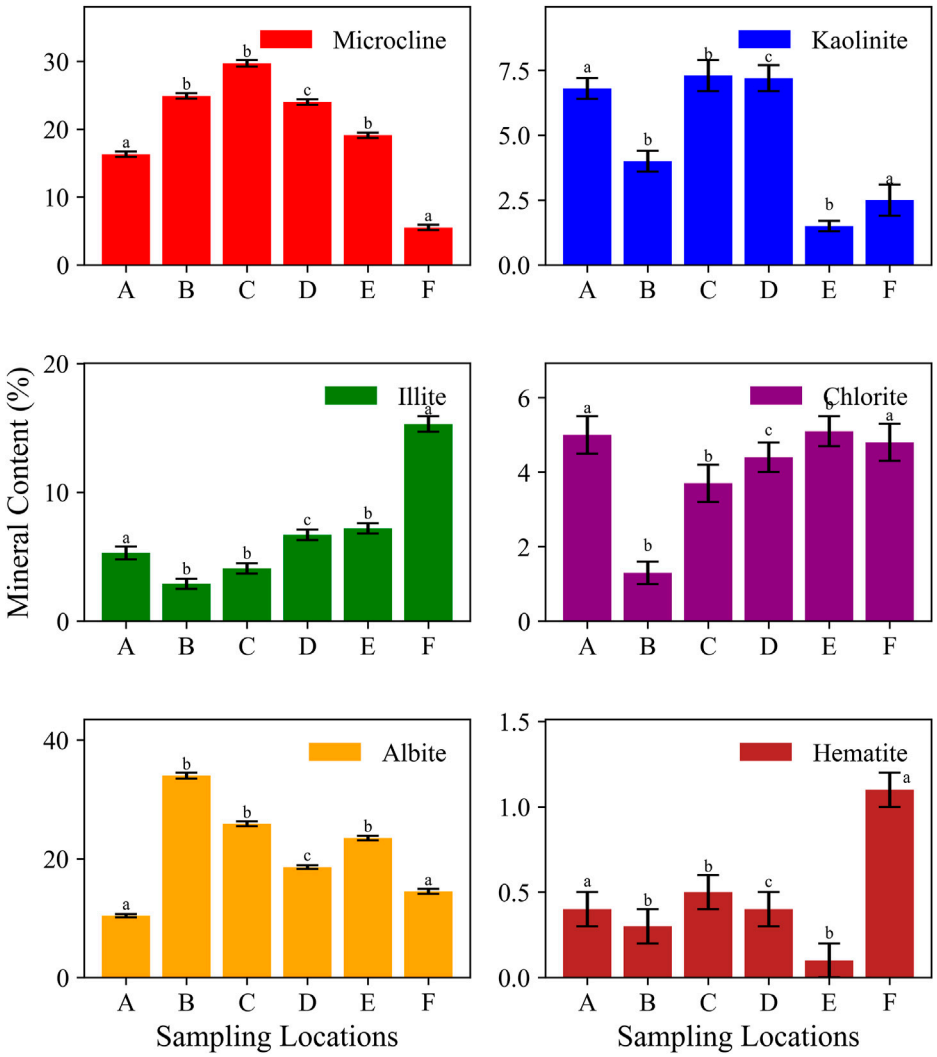

FIGURE 12
Mineral content distribution across sampling locations A to F; error bars indicate ±SE. Different lowercase letters above bars denote significant differences among sites (Tukey's HSD, α = 0.05): a ($p < 0.01$), b ($p < 0.05$), c ($p < 0.10$).

with moderate enrichment in C–N, pyridinic-N, and aromatic structures, suggesting a transitional biogeochemical zone. High-elevation sites (E and F) showed pronounced accumulation of polar (O–H/N–H) and aromatic nitrogen groups, higher Fe^{3+} levels, and abundant clay minerals (e.g., illite, chlorite), reflecting enhanced organic–mineral interactions, advanced humification, and greater carbon stabilization. Functional clustering further supported this pattern, identifying two major modules: one linked to polar groups and minerals, and the other to aromatic and nitrogen-rich structures—highlighting a systematic shift in organic matter composition and stability with elevation. The results indicate significant differences in elemental distribution, chemical forms, and ecological functions of microaggregates across three elevation zones: low, middle, and high (Table 5).

Low-elevation zone (<600 m): In the low-elevation soils, microaggregates showed surface enrichment of heavy metals to an anomalously high degree. For instance, at site A the microaggregate surface Fe content reached ~3.37% and Mn ~1.61% (by XPS), exceeding levels expected from natural rock weathering. These abnormally high metal concentrations, when considered alongside local land use and pollution data, point to substantial exogenous metal inputs in the low-elevation area. Likely sources include industrial emissions, vehicular traffic dust, and agricultural activities from the surrounding region (McCrackin et al., 2017; Xu X. et al., 2022). SEM-EDS and XRF analyses further confirmed that this metal enrichment was mostly confined to the microaggregate surfaces and did not extend into the interior of aggregates or deeper soil, indicating recent surface loading (Duiker et al., 2003). Among the metals, Fe in the low zone was predominantly in the reduced form (Fe^{2+}), accompanied by localized Mn hotspots—reflecting a reducing soil microenvironment with high metal mobility (Chacon et al., 2018). Multivariate analysis highlighted that at low elevation, microaggregates form a distinct cluster driven by these exogenous input-driven surface metal accumulations, which greatly increase the risk of metal loss via runoff or erosion (Figures 15, 16). This conclusion is supported by Malunguja et al. (2022), who found that forest soils near highways

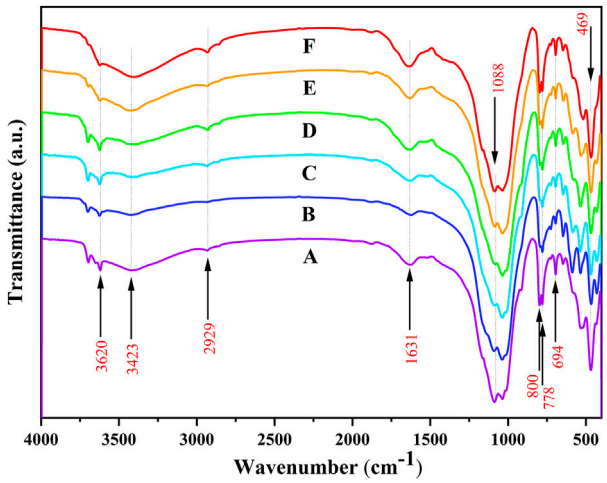

FIGURE 13
FTIR spectrum with characteristic absorption peaks across sampling locations A to F.

accumulated elevated levels of Cd, Mn, and Pb in their surface layers, with concentrations positively correlated with traffic density. Similarly, our low-elevation findings underscore that human activities can create a "loaded" surface soil system prone to heavy-metal migration.

Mid-elevation zone (~600–700 m): The mid-elevation microaggregates exhibited transitional features between the polluted low zone and the accumulative high zone. XPS and SEM-EDS results showed higher phosphorus content and clay mineral abundance in these soils, alongside an increase in Fe^{3+} relative to Fe^{2+}. This suggests more oxidizing conditions and stable iron oxide formation at mid elevation (Duiker et al., 2003). The relatively dense vegetation cover and moderate weathering intensity in this zone appear to promote the formation of mineral–organic complexes (for example, clays coated with humus and iron oxides). Meanwhile, active microbial processes help maintain a balance: nutrients like P and N released by weathering and decomposition are rapidly taken up or stabilized, while heavy metals are either sequestered in stable aggregates or kept in forms that do not easily mobilize. In other words, mid elevations seem to strike a synergistic balance between biological activity and geochemical weathering, which supports nutrient retention (preventing leaching of P, N, etc.) and limits heavy-metal transport. This balance is reflected in the stability of microaggregates and the relatively low ecological risk observed in this zone. Such mechanisms are consistent with the framework proposed by Lehmann and Kleber (2015), who emphasized the role of organo-mineral associations in nutrient and metal retention, and with field observations by Finlay et al. (2020) in mountainous catchments where intermediate elevations often maintain high soil fertility while mitigating metal mobility.

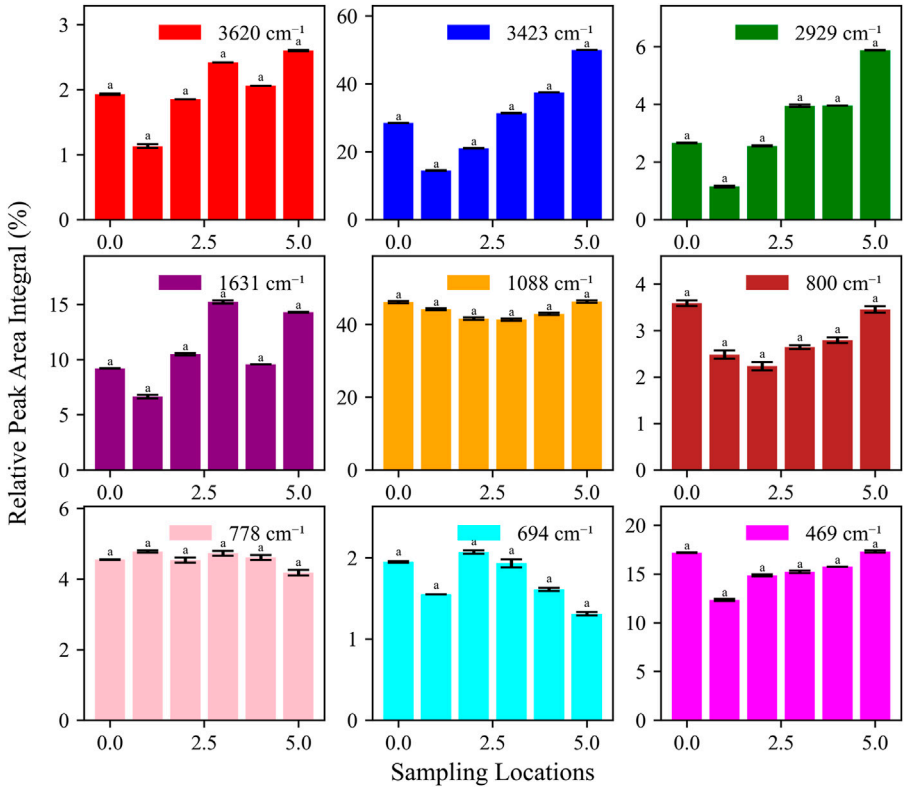

FIGURE 14
Relative peak area integrals of FTIR spectra at different wavenumbers across sampling locations A to F; error bars indicate ±SE. Different lowercase letters above bars denote significant differences among sites (Tukey's HSD, α = 0.05): a ($p < 0.01$), b ($p < 0.05$), c ($p < 0.10$).

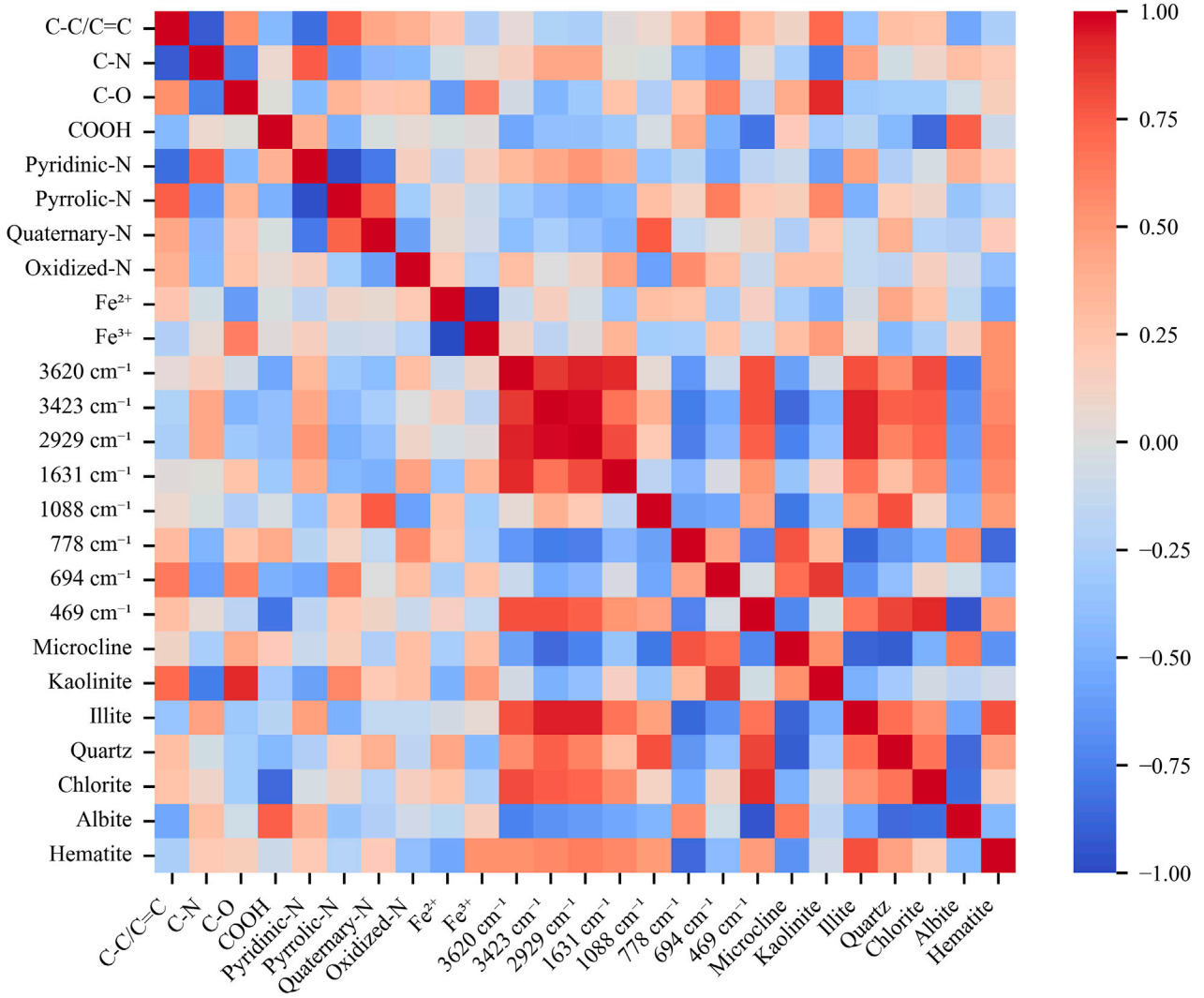

FIGURE 15
Correlation matrix of elemental, FTIR spectra and mineral content across sampling locations A to F.

High-elevation zone (>700 m): The high-elevation sites (E and F) were characterized by element fixation and accumulation in microaggregates. XPS and FTIR analyses showed significant increases in soil organic carbon content and a high degree of humification in these soils. We observed enhanced levels of functional groups indicative of stable organic matter (e.g., strong peaks for–OH, –NH, COOH, and aromatic N at these sites) (Cao et al., 2022). Iron speciation at high elevation was dominated by Fe^{3+} (with only minor Fe^{2+}), facilitating the formation of stable organo–metal complexes–for example, aromatic organic compounds bonding with Fe^{3+} and even Mn^{2+} (Witzgall et al., 2021). SEM-EDS images corroborated this, revealing tightly packed microaggregates with extensive coatings of iron oxides and clays bound to organic matter. We also noted a significant buildup of weathering-resistant minerals like Ti oxides in the high-elevation microaggregates (Tan et al., 2018), which is expected given the intense leaching of more soluble components over time. The cold, wet environment at these upper elevations greatly slows down organic matter decomposition, allowing organic material to accumulate and undergo thorough humification. The net effect at high elevation is a soil that functions as both a "carbon sink" and a "heavy metal sink." The higher content of minerals, such as illite and chlorite, at high elevations passivates heavy metals through adsorption (Figure 12), complexation, and co-precipitation, reducing the activity and bioavailability of heavy metals in surface soil and reducing their mobility (Huang et al., 2023; Escobar et al., 2024). This dual sink behavior has been observed in other mountain systems as well (Tsozué et al., 2019; Li et al., 2022; Apori et al., 2024). It indicates that above a certain elevation, natural soils can effectively sequester carbon and pollutants, provided the environment remains undisturbed.

Across the entire gradient, our analyses indicate that elevation regulates soil organic carbon accumulation and heavy-metal dynamics primarily via changes in temperature, moisture, and vegetation. The critical threshold appears around 600–700 m (Figure 16). Below ~600 m, soils experience greater anthropogenic influence and more reducing conditions, leading to higher heavy-metal bioavailability and ecological risk. Above

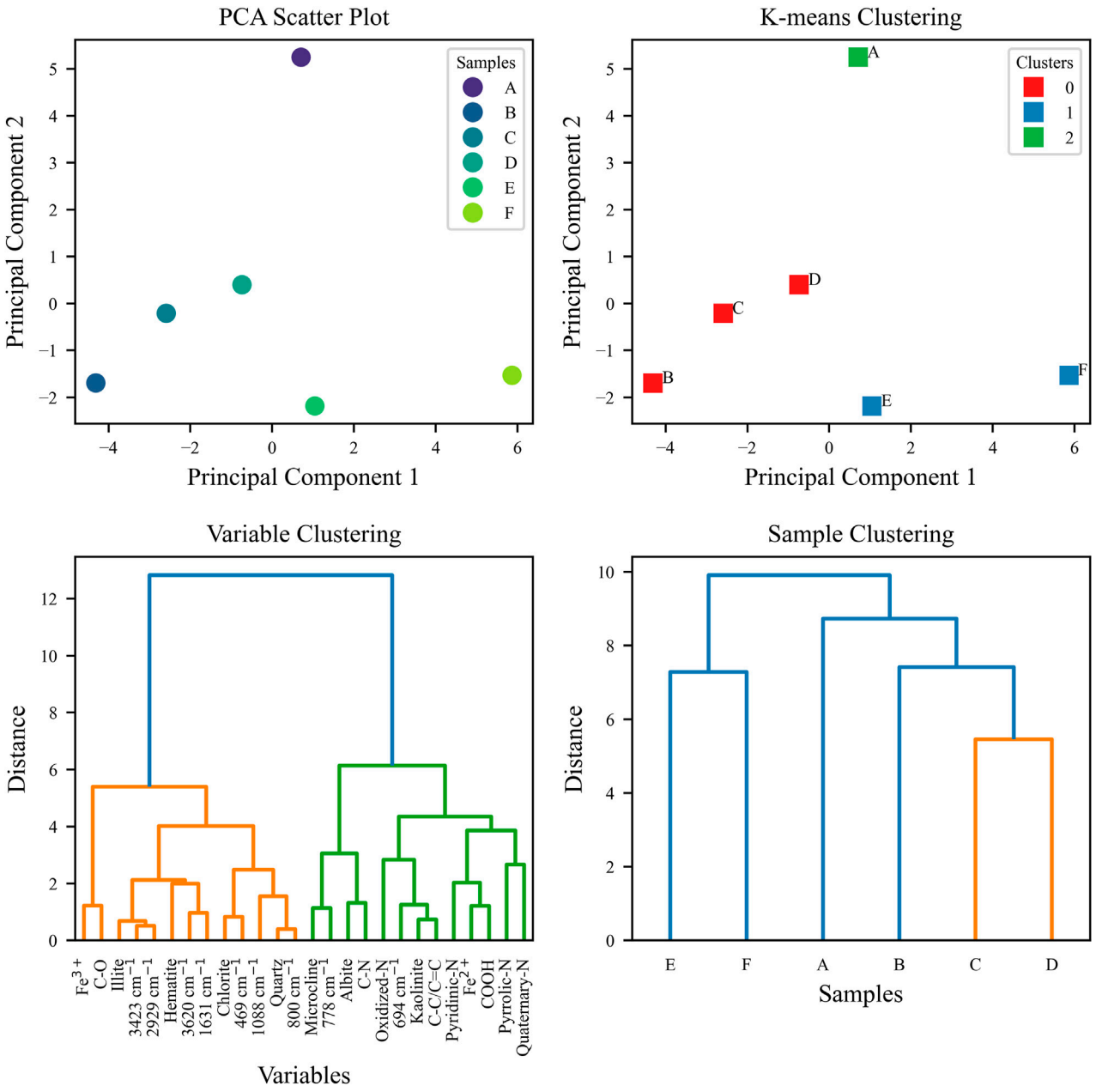

FIGURE 16
Multivariate analysis: PCA, K-means clustering, and Hierarchical clustering of variables and samples.

~700 m, soils exhibit higher metal fixation capacity and lower bioavailability, corresponding with the emergence of mature forests and different soil types. This ~600–700 m pivot coincides with major changes in vegetation (from agricultural/secondary growth to native forest) and soil taxonomy, reflecting the combined effects of climate and geology at this transition (Tsozué et al., 2019).

Based on these findings, we propose differentiated management strategies for the various elevation zones in Tongbai Mountain. Low elevations (<600 m): Strengthen controls on external pollution sources and optimize land use to reduce heavy-metal inputs. Improving soil structure and microaggregate stability (for instance, through organic amendments) can help immobilize metals and reduce their runoff. Mid elevations (≈600–700 m): Protect and maintain vegetation cover to sustain the natural balance of weathering and biological nutrient cycling. A healthy vegetation layer will promote mineral–organic complex formation and nutrient retention, as also suggested by Lehmann and Kleber (2015), thereby keeping heavy metals bound in stable soil aggregates. High elevations (>700 m): Conserve the intact natural ecosystems and soil structure to preserve the soils' role as carbon and metal sinks. It is also crucial to monitor these areas for any signs of heavy-metal release under climate warming (Kleber et al., 2021) and to manage factors (like erosion or permafrost thaw, if applicable) that could disturb

TABLE 5 Elemental, morphological, and environmental profiles of soil microaggregates along the elevation gradient.

Site (elev.)	Elemental distribution	Chemical morphology	Environmental conditions
A (Low-elevation)	Fe 3.37% (lower), Mn 1.61% (peak, Mn oxides), Ti 1.07% (higher), C 22.96%, N 1.79% (low organic content), P 1.03% (anthropogenic depletion)	Fe^{2+}-rich (~49.3% Fe^{2+}); very low C–N bond fraction (~19.2%); minimal Pyridinic-N (~21.1%); high C–C/C=C (~54.5%) indicates fresh, unoxidized carbon	Foot-slope, water-logged and reducing; strong anthropogenic input limits P retention; humus formation minimal ⇒ high Mn/Fe mobility
B (Low-elevation)	Fe 3.36%, Mn 1.12%, Ti 1.06%, C 21.12%, N 2.05%, P 0.95%	Fe^{2+}-rich (~46.1% Fe^{2+}); C–N bond fraction (~22.8%); elevated Pyridinic-N (~37.2%); C–C/C=C (~48.1%) indicates fresh, unoxidized carbon	Low-elevation farmland under continued reduction; P depleted, rapid C turnover; metals remain mobile, pollutant-leaching risk persists
C (Mid-elevation)	Fe 3.72% (increasing), Mn 0.87% (low), Ti 1.04%, C 22.99%, N 1.89%, P 1.05% (elevated)	Fe^{3+} dominant (~62.4% Fe^{3+}); rising C–N bond content (~24.6%); Pyridinic-N stable high (~37.0%); lower C–C/C=C (~48.4%) and higher C–O (~15.6%) signal increasing oxidation	Mid-elevation transition—well-drained, oxidising; weathering and bioturbation boost nutrients; metal retention strengthens as Fe oxides form
D (Mid-elevation)	Fe 2.81% (decreasing), Mn 1.13% (stable), Ti 0.95%, C 27.86%, N 2.19% (richer organic matter), P 1.04%	Fe^{3+} strong (~55.7% Fe^{3+}); moderate C–N bonds (~20.2%); higher Pyridinic-N (~40.2%); elevated COOH (~12.1%) marks advanced humification and carboxylation	Upper mid-elevation, strongly oxidising; efficient nutrient capture, advanced humification; soils act as effective metal–nutrient sinks
E (High-elevation)	Fe 4.35% (high), Mn 1.00%, Ti 0.90%, C 23.70%, N 2.37% (max), P 0.94% (moderate)	Fe^{2+}/Fe^{3+} mixed (~52.4% Fe^{2+} pockets); highest C–N bond content (~27.1%); high Pyridinic-N (~44.1%); declining C-O (~13.8%) suggests stabilized aromatic humus	Cold, wet highland with thick organic layer; strong C/metal sequestration within organo-Fe(III) complexes
F (High-elevation)	Fe 4.93% (highest), Mn 1.19%, Ti 1.15% (highest), C 23.33%, N 2.13%, P 1.43% (inorganic)	Fe^{3+} dominant (~57.2% Fe^{3+}); high C–N (~26.4%); maximum Pyridinic-N (~44.4%); lowest C-C/C=C (~46.8%) and lowest oxidized-N (~10.8%) reflect peak humification and organo-Fe(III) complex formation	Cool, humid summit; highly humified organic matter; robust Fe(III)–organic matrices lock in C and metals—soil functions as long-term sink

the stabilized organo-mineral complexes. Implementing these targeted strategies will provide a scientific basis for the ecological protection of Tongbai Mountain and the sustainable management of its mountain ecosystems. In particular, as global climate change continues, the high-elevation soils should be closely observed: warming temperatures may threaten to destabilize the stored carbon and heavy metals, highlighting the need for proactive monitoring and adaptive measures to maintain the current sink functions of these soils.

5 Conclusion

Our elevation-gradient survey of Tongbai Mountain (200–1,140 m) reveals a clear altitudinal hierarchy in soil microaggregate chemistry and function. Low elevations (<600 m) are dominated by surface-enriched Mn and Fe (XPS Mn ≈ 1.6%, Fe ≈ 3.4% at 200 m), indicative of anthropogenic inputs and reducing conditions that enhance metal mobility. At mid-slope elevations (600–700 m), P and Al reach local maxima, marking a zone of intense weathering and biotic turnover. Above 700 m, cooler and wetter conditions promote the formation of organo-mineral complexes that sequester C, N, and Fe. The C–N spectral component nearly doubles from 19.2% at 200 m to 26.4% at 1,140 m, while pyridinic-N increases from 21.1% to 44.4%. Meanwhile, iron shifts to a Fe^{3+}-dominated pool, indicating enhanced humification and oxidative weathering at higher elevations.

These chemical transitions translate into contrasting ecosystem services. Robust organic-matter–mineral associations at high elevations stabilise carbon and immobilise metals through complexation with–OH and–COOH groups, producing effective "carbon and metal sinks". By contrast, weaker aggregates and continuous disturbance at low elevations leave anthropogenic metals—particularly Mn—mobile and ecologically hazardous. The 600–700 m band emerges as a biogeochemical tipping point: below it, carbon losses and heavy-metal transport risk escalate; above it, soils buffer both carbon and metals. Management must therefore be stratified. Lowlands require stringent pollution control and measures that promote aggregate stability; mid-slopes benefit from vegetation reinforcement to sustain nutrient cycling; high-elevation refugia demand protection and long-term monitoring, especially as climate warming could accelerate organic-matter decay and release sequestered metals. By integrating elevation as a key variable in carbon and pollution mitigation strategies, our study establishes a mechanistic framework for anticipating and mitigating the effects of climate warming and altered precipitation regimes on mountain soils within China's north–south climatic transition zone.

Data availability statement

The original contributions presented in the study are included in the article/supplementary material, further inquiries can be directed to the corresponding author.

Author contributions

CL: Project administration, Validation, Visualization, Writing – original draft, Methodology, Formal Analysis,

Software, Data curation, Writing – review and editing, Resources, Conceptualization, Investigation. SG: Software, Data curation, Funding acquisition, Validation, Writing – review and editing, Methodology.

Funding

The author(s) declare that no financial support was received for the research and/or publication of this article.

Conflict of interest

The authors declare that the research was conducted in the absence of any commercial or financial relationships that could be construed as a potential conflict of interest.

Generative AI statement

The author(s) declare that no Generative AI was used in the creation of this manuscript.

Any alternative text (alt text) provided alongside figures in this article has been generated by Frontiers with the support of artificial intelligence and reasonable efforts have been made to ensure accuracy, including review by the authors wherever possible. If you identify any issues, please contact us.

Publisher's note

References

Amelung, W., Tang, N., Siebers, N., Aehnelt, M., Eusterhues, K., Felde, V. J. M. N. L., et al. (2024). Architecture of soil microaggregates: advanced methodologies to explore properties and functions. *J. Plant Nutr. Soil Sci.* 187 (1), 17–50. doi:10.1002/JPLN.202300149

Apori, S. O., Giltrap, M., Dunne, J., and Tian, F. (2024). Human health and ecological risk assessment of heavy metals in topsoil of different peatland use types. *Heliyon* 10 (13), E33624. doi:10.1016/J.HELIYON.2024.E33624

Barber, K. L., Maddux, L. D., Kissel, D. E., Pierzynski, G. M., and Bock, B. R. (1992). Corn responses to ammonium- and nitrate-nitrogen fertilization. *Soil Sci. Soc. Am. J.* 56 (4), 1166–1171. doi:10.2136/SSSAJ1992.03615995005600040027X

Bravo-Medina, C., Torres-Navarrete, B., Arteaga-Crespo, Y., Garcia-Quintana, Y., Reyes-Morán, H., Changoluisa-Vargas, D., et al. (2023). Soil properties variation in a small-scale altitudinal gradient of an evergreen foothills forest, Ecuadorian amazon region. *Eur. J. For. Res.* 142 (6), 1325–1339. doi:10.1007/S10342-023-01593-6

Calderón, F., Haddix, M., Conant, R., Magrini-Bair, K., and Paul, E. (2013). Diffuse-reflectance Fourier-transform mid-infrared spectroscopy as a method of characterizing changes in soil organic matter. *Soil Sci. Soc. Am. J.* 77 (5), 1591–1600. doi:10.2136/SSSAJ2013.04.0131

Cao, D., Hao, Q., Sun, R., Wang, Y., Zhang, Y., and Zhou, H. (2022). Multiple stoichiometric methods combined with FT-IR spectroscopy for screening new medicinal parts from Dictamnus dasycarpus Turcz with pronounced antioxidant potential. *J. Mol. Struct.* 1252, 132187. doi:10.1016/J.MOLSTRUC.2021.132187

Chacon, S. S., García-Jaramillo, M., Liu, S. Y., Ahmed, M., and Kleber, M. (2018). Differential capacity of kaolinite and birnessite to protect surface associated proteins against thermal degradation. *Soil Biol. biochem.* 119, 101–109. doi:10.1016/J.SOILBIO.2018.01.020

Chen, Y., Glaus, M. A., Van Loon, L. R., and Mäder, U. (2018). Transport of low molecular weight organic compounds in compacted illite and kaolinite. *Chemosphere* 198, 226–237. doi:10.1016/J.CHEMOSPHERE.2018.01.137

Chen, C., Hall, S. J., Coward, E., and Thompson, A. (2020). Iron-mediated organic matter decomposition in humid soils can counteract protection. *Nat. Commun.* 11 (1), 2255. doi:10.1038/S41467-020-16071-5

Chen, X., Feng, J., Ding, Z., Tang, M., and Zhu, B. (2022). Changes in soil total, microbial and enzymatic C-N-P contents and stoichiometry with depth and latitude in forest ecosystems. *Sci. Total Environ.* 816, 151583. doi:10.1016/j.scitotenv.2021.151583

Choudhury, B. U., Fiyaz, A. R., Mohapatra, K. P., and Ngachan, S. (2016). Impact of land uses, agrophysical variables and altitudinal gradient on soil organic carbon concentration of north-eastern Himalayan region of India. *L. Degrad. Dev.* 27 (4), 1163–1174. doi:10.1002/LDR.2338

Dan, W., Nianpeng, H., Qing, W., Yuliang, L., Qiufeng, W., Zhiwei, X., et al. (2016). Effects of temperature and moisture on soil organic matter decomposition along elevation gradients on the Changbai Mountains, Northeast China. *Pedosphere* 26 (3), 399–407. doi:10.1016/S1002-0160(15)60052-2

Duan, D., Wang, P., Rao, X., Zhong, J., Xiao, M., Huang, F., et al. (2024). Identifying interactive effects of spatial drivers in soil heavy metal pollutants using interpretable machine learning models. *Sci. Total Environ.* 934, 173284. doi:10.1016/J.SCITOTENV.2024.173284

Duiker, S. W., Rhoton, F. E., Torrent, J., Smeck, N. E., and Lal, R. (2003). Iron (Hydr) oxide crystallinity effects on soil aggregation. *Soil Sci. Soc. Am. J.* 67 (2), 606–611. doi:10.2136/SSSAJ2003.6060

Dunlea, A. G., Murray, R. W., Tada, R., Alvarez-Zarikian, C. A., Anderson, C. H., Gilli, A., et al. (2020). Intercomparison of XRF core scanning results from seven labs and approaches to practical calibration. *Geochem. Geophys. Geosystems.* 21 (9), e2020GC009248. doi:10.1029/2020GC009248

Ersoy, O., Aydar, E., Gourgaud, A., and Bayhan, H. (2008). Quantitative analysis on volcanic ash surfaces: application of extended depth-of-field (focus) algorithm for light and scanning electron microscopy and 3D reconstruction. *Micron* 39 (2), 128–136. doi:10.1016/J.MICRON.2006.11.010

Escobar, M., Ji, J., Wang, Y., Feng, M., Bao, C., Ma, J., et al. (2024). Effect of thermal treatment of illite on the bioavailability of copper and zinc in the aerobic composting of pig manure with corn straw. *Front. Microbiol.* 15, 1411251. doi:10.3389/FMICB.2024.1411251

Finlay, R. D., Mahmood, S., Rosenstock, N., Bolou-Bi, E. B., Köhler, S. J., Fahad, Z., et al. (2020). Reviews and syntheses: biological weathering and its consequences at different spatial levels: from nanoscale to global scale. *Biogeosciences* 17 (6), 1507–1533. doi:10.5194/BG-17-1507-2020

Guidi, P., Falsone, G., Wilson, C., Cavani, L., Ciavatta, C., and Marzadori, C. (2021). New insights into organic carbon stabilization in soil macroaggregates: an *in situ* study by optical microscopy and SEM-Eds technique. *Geoderma* 397, 115101. doi:10.1016/J.GEODERMA.2021.115101

He, X., Hou, E., Liu, Y., and Wen, D. (2016). Altitudinal patterns and controls of plant and soil nutrient concentrations and stoichiometry in subtropical China. *Sci. Rep.* 6, 24261. doi:10.1038/SREP24261

Huang, H., Shi, L., Chen, R., and Yuan, J. (2023). Effect of modified illite on Cd immobilization and fertility enhancement of acidic soils. *Sustainability* 15 (6), 4950. doi:10.3390/SU15064950

Igwe, C. A., Zarei, M., and Stahr, K. (2005). Mineral and elemental distribution in soils formed on the river niger floodplain, eastern Nigeria. *Aust. J. Soil Res.* 43 (2), 147–158. doi:10.1071/SR04046

Ivashchenko, K., Sushko, S., Selezneva, A., Ananyeva, N., Zhuravleva, A., Kudeyarov, V., et al. (2021). Soil microbial activity along an altitudinal gradient: vegetation as a main driver beyond topographic and edaphic factors. *Appl. Soil Ecol.* 168, 104197. doi:10.1016/J.APSOIL.2021.104197

Jiang, C., Shi, T., Mo, Z., and Zhao, C. (2024). Across a phylogeographic break in the qinling mountains-Huaihe river line: quaternary evolutionary history of a medicinal and edible homologous plant (*Allium macrostemon*) in China. *BMC Ecol. Evol.* 24 (1), 107. doi:10.1186/S12862-024-02297-0

Jindo, K., Audette, Y., Olivares, F. L., Canellas, L. P., Smith, D. S., and Paul Voroney, R. (2023). Biotic and abiotic effects of soil organic matter on the phytoavailable phosphorus in soils: a review. *Chem. Biol. Technol. Agric.* 10 (1), 29. doi:10.1186/S40538-023-00401-Y

Keller, A. B., Borer, E. T., Collins, S. L., DeLancey, L. C., Fay, P. A., Hofmockel, K. S., et al. (2022). Soil carbon stocks in temperate grasslands differ strongly across sites but are insensitive to decade-long fertilization. *Glob. Chang. Biol.* 28 (4), 1659–1677. doi:10.1111/GCB.15988

Kleber, M., Bourg, I. C., Coward, E. K., Hansel, C. M., Myneni, S. C. B., and Nunan, N. (2021). Dynamic interactions at the mineral–organic matter interface. *Nat. Rev. Earth Environ.* 2 (6), 402–421. doi:10.1038/S43017-021-00162-Y

Kong, A. Y. Y., Scow, K. M., Córdova-Kreylos, A. L., Holmes, W. E., and Six, J. (2011). Microbial community composition and carbon cycling within soil microenvironments of conventional, low-input, and organic cropping systems. *Soil Biol. biochem.* 43 (1), 20–30. doi:10.1016/J.SOILBIO.2010.09.005

Kuzyakov, Y., and Blagodatskaya, E. (2015). Microbial hotspots and hot moments in soil: concept and review. *Soil Biol. biochem.* 83, 184–199. doi:10.1016/J.SOILBIO.2015.01.025

Lehmann, J., and Kleber, M. (2015). The contentious nature of soil organic matter. *Nature* 528 (7580), 60–68. doi:10.1038/NATURE16069

Lehmann, J., Hansel, C. M., Kaiser, C., Kleber, M., Maher, K., Manzoni, S., et al. (2020). Persistence of soil organic carbon caused by functional complexity. *Nat. Geosci.* 13 (8), 529–534. doi:10.1038/S41561-020-0612-3

Li, C., and Guo, S. (2022). Structural evolution of soil aggregates in a karst rocky desertification area. *RSC Adv.* 12 (33), 21004–21013. doi:10.1039/D2RA02901D

Li, L., Vogel, J., He, Z., Zou, X., Ruan, H., Huang, W., et al. (2016). Association of soil aggregation with the distribution and quality of organic carbon in soil along an elevation gradient on wuyi Mountain in China. *PLoS ONE* 11 (3), e0150898. doi:10.1371/JOURNAL.PONE.0150898

Li, Q., Wang, Y., Li, Y., Li, L., Tang, M., Hu, W., et al. (2022). Speciation of heavy metals in soils and their immobilization at micro-scale interfaces among diverse soil components. *Sci. Total Environ.* 825, 153862. doi:10.1016/J.SCITOTENV.2022.153862

Li, C., Guo, S., Shang, S., Qi, P., and Li, B. (2023a). Structure and biogeochemical process of microaggregates in a water source area of China's south-to-north water diversion project according to different land use types. *Front. Environ. Sci.* 11, 1165454. doi:10.3389/FENVS.2023.1165454

Li, Q., Wang, L., Fu, Y., Lin, D., Hou, M., Li, X., et al. (2023b). Transformation of soil organic matter subjected to environmental disturbance and preservation of organic matter bound to soil minerals: a review. *J. Soils Sediments* 23 (3), 1485–1500. doi:10.1007/S11368-022-03381-Y

Li, C., Xu, W., Guo, S., Shang, S., and Li, B. L. (2024a). Impact of gradient zero-valent iron pollution from steel works on soil microaggregate geochemical processes and dissipative structures. *Front. Environ. Sci.* 12, 1470746. doi:10.3389/FENVS.2024.1470746

Li, X., Schindler, M., Zhou, J., Samaradiwakara, S., and Wu, L. (2024b). Interaction between metal(loid)s and soil mineral-organic matter associations. *Crit. Rev. Environ. Sci. Technol.* 54, 624–647. doi:10.1080/10643389.2024.2434328

Li, C., Guo, S., and Shang, S. (2025). Synergistic evolution of soil microaggregates biogeochemical processes driven by elevation gradients in tongbai Mountain. *PLOS ONE* 20 (6), e0325425. doi:10.1371/journal.pone.0325425

Liu, Y. L., Yao, S. H., Han, X. Z., Zhang, B., and Banwart, S. A. (2017). Soil mineralogy changes with different agricultural practices during 8-year soil development from the parent material of a mollisol. *Adv. Agron.* 142, 143–179. doi:10.1016/BS.AGRON.2016.10.015

Lyu, S., Wei, X., Chen, J., Wang, C., Wang, X., and Pan, D. (2017). Titanium as a beneficial element for crop production. *Front. Plant Sci.* 8, 597. doi:10.3389/FPLS.2017.00597

Malunguja, G. K., Thakur, B., and Devi, A. (2022). Heavy metal contamination of forest soils by vehicular emissions: ecological risks and effects on tree productivity. *Environ. Process.* 9 (1), 11. doi:10.1007/S40710-022-00567-X

Martens, J., Mueller, C. W., Joshi, P., Rosinger, C., Maisch, M., Kappler, A., et al. (2023). Stabilization of mineral-associated organic carbon in Pleistocene permafrost. *Nat. Commun.* 14 (1), 2120. doi:10.1038/S41467-023-37766-5

McCrackin, M. L., Jones, H. P., Jones, P. C., and Moreno-Mateos, D. (2017). Recovery of Lakes and coastal marine ecosystems from eutrophication: a global meta-analysis. *Limnol. Oceanogr.* 62 (2), 507–518. doi:10.1002/LNO.10441

Newbury, D., Ritchie, N., Mengason, M., and Scott, K. (2017). SEM/Eds trace analysis: limits imposed by fluorescence of the detector. *Microsc. Microanal.* 23 (S1), 1026–1027. doi:10.1017/S1431927617005797

Nottingham, A. T., Fierer, N., Turner, B. L., Whitaker, J., Ostle, N. J., McNamara, N. P., et al. (2018). Microbes follow humboldt: temperature drives plant and soil microbial diversity patterns from the amazon to the andes. *Ecology* 99 (11), 2455–2466. doi:10.1002/ECY.2482

Possinger, A. R., Zachman, M. J., Enders, A., Levin, B. D. A., Muller, D. A., Kourkoutis, L. F., et al. (2020). Organo–organic and organo–mineral interfaces in soil at the nanometer scale. *Nat. Commun.* 11 (1), 6103. doi:10.1038/S41467-020-19792-9

Salim, Z., Khan, M. U., and Malik, R. N. (2020). Concentration, distribution and association of heavy metals in multi-matrix samples of himalayan foothill along elevation gradients. *Environ. Earth Sci.* 79 (20), 479. doi:10.1007/S12665-020-09218-6

Shaheen, S. M., Alessi, D. S., Tack, F. M. G., Ok, Y. S., Kim, K. H., Gustafsson, J. P., et al. (2019). Redox chemistry of vanadium in soils and sediments: interactions with colloidal materials, mobilization, speciation, and relevant environmental implications: a review. *Adv. Colloid Interface Sci.* 265, 1–13. doi:10.1016/J.CIS.2019.01.002

Shirshova, L. T., Ghabbour, E. A., and Davies, G. (2006). Spectroscopic characterization of humic acid fractions isolated from soil using different extraction procedures. *Geoderma* 133 (3-4), 204–216. doi:10.1016/J.GEODERMA.2005.07.007

Singh, V., and Agrawal, H. M. (2012). Qualitative soil mineral analysis by EDXRF, XRD and AAS probes. *Radiat. Phys. Chem.* 81 (12), 1796–1803. doi:10.1016/J.RADPHYSCHEM.2012.07.002

Sokol, N. W., Whalen, E. D., Jilling, A., Kallenbach, C., Pett-Ridge, J., and Georgiou, K. (2022). Global distribution, formation and fate of mineral-associated soil organic matter under a changing climate: a trait-based perspective. *Funct. Ecol.* 36 (6), 1411–1429. doi:10.1111/1365-2435.14040

Solymos, K., Babcsányi, I., Ariya, B., Gyulavári, T., Ágoston, Á., Kukovecz, Á., et al. (2024). Environmental significance of the interaction between titanium dioxides and soil solutions. *Environ. Sci. Eur.* 36 (1), 85. doi:10.1186/S12302-024-00903-Y

Song, J., Brookes, P. C., Shan, S., Xu, J., and Liu, X. (2022). Effects of remediation agents on microbial community structure and function in soil aggregates contaminated with heavy metals. *Geoderma* 425, 116030. doi:10.1016/J.GEODERMA.2022.116030

Sun, P., Sun, Y., Zhang, Q., and Yao, R. (2018). Hydrological processes in the huaihe river basin, China: seasonal variations, causes and implications. *Chin. Geogr. Sci.* 28 (4), 636–653. doi:10.1007/S11769-018-0969-Z

Tan, W., Peralta-Videa, J. R., and Gardea-Torresdey, J. L. (2018). Interaction of titanium dioxide nanoparticles with soil components and plants: current knowledge and future research needs-a critical review. *Environ. Sci. Nano* 5 (2), 257–278. doi:10.1039/C7EN00985B

Tang, J., Zhao, J., Qin, Z., Chen, L., Song, X., Ke, Q., et al. (2023). Structural equation model was used to evaluate the effects of soil chemical environment, fertility and enzyme activity on eucalyptus biomass. *R. Soc. Open Sci.* 10 (4), 221570. doi:10.1098/RSOS.221570

Totsche, K. U., Amelung, W., Gerzabek, M. H., Guggenberger, G., Klumpp, E., Knief, C., et al. (2018). Microaggregates in soils. *J. Plant Nutr. Soil Sci.* 181 (1), 104–136. doi:10.1002/JPLN.201600451

Tsozué, D., Nghonda, J. P., Tematio, P., and Basga, S. D. (2019). Changes in soil properties and soil organic carbon stocks along an elevation gradient at mount bambouto, Central Africa. *Catena* 175, 251–262. doi:10.1016/J.CATENA.2018.12.028

Wang, H. C., Chou, C. Y., Chiou, C. R., Tian, G., and Chiu, C. Y. (2016). Humic acid composition and characteristics of soil organic matter in relation to the elevation gradient of moso bamboo plantations. *PLoS ONE* 11 (9), e0162193. doi:10.1371/JOURNAL.PONE.0162193

Wang, J. L., Alasonati, E., Fisicaro, P., and Benedetti, M. F. (2022). Titanium nanoparticles fate in small-sized watersheds under different land-uses. *J. Hazard. Mat.* 422, 126695. doi:10.1016/J.JHAZMAT.2021.126695

Wang, H., Feng, R., Li, X., Yang, Y., and Pan, Y. (2023). Land use change and its impact on ecological risk in the Huaihe river eco-economic belt. *Land* 12 (6), 1247. doi:10.3390/LAND12061247

Wasner, D., Abramoff, R., Griepentrog, M., Venegas, E. Z., Boeckx, P., and Doetterl, S. (2024). The role of climate, mineralogy and stable aggregates for soil organic carbon dynamics along a geoclimatic gradient. *Glob. Biogeochem. Cycles* 38 (7), e2023GB007934. doi:10.1029/2023GB007934

Witzgall, K., Vidal, A., Schubert, D. I., Höschen, C., Schweizer, S. A., Buegger, F., et al. (2021). Particulate organic matter as a functional soil component for persistent soil organic carbon. *Nat. Commun.* 12 (1), 4115. doi:10.1038/S41467-021-24192-8

Wu, M., Pang, D., Chen, L., Li, X., Liu, L., Liu, B., et al. (2021). Chemical composition of soil organic carbon and aggregate stability along an elevation gradient in helan Mountains, northwest China. *Ecol. Indic.* 131, 108228. doi:10.1016/J.ECOLIND.2021.108228

Xiao, K. Q., Zhao, Y., Liang, C., Zhao, M., Moore, O. W., Otero-Fariña, A., et al. (2023). Introducing the soil mineral carbon pump. *Nat. Rev. Earth Environ.* 4 (3), 135–136. doi:10.1038/S43017-023-00396-Y

Xiao, W., Zhang, Y., Chen, X., Sha, A., Xiong, Z., Luo, Y., et al. (2024). The easily overlooked effect of global warming: diffusion of heavy metals. *Toxics* 12 (6), 400. doi:10.3390/toxics12060400

Xu, X., Wu, Y., Wu, X., Sun, Y., Huang, Z., Li, H., et al. (2022a). Effect of physicochemical properties of biochar from different feedstock on remediation of heavy metal contaminated soil in mining area. *Surfaces Interfaces* 32, 102058. doi:10.1016/J.SURFIN.2022.102058

Xu, Y., Liu, K., Yao, S., Zhang, Y., Zhang, X., He, H., et al. (2022b). Formation efficiency of soil organic matter from plant litter is governed by clay mineral type more than plant litter quality. *Geoderma* 412, 115727. doi:10.1016/J.GEODERMA.2022.115727

Yang, N., Zhou, C., Li, Y., and Deng, Y. (2025). Microbial specialists in high-altitude forest soils: environmental sensitivity and ecological significance. *Front. Environ. Sci. Eng.* 19 (3), 30. doi:10.1007/S11783-025-1950-6

Yin, S., Wang, C., and Zhou, Z. (2022). Globally altitudinal trends in soil carbon and nitrogen storages. *Catena* 210, 105870. doi:10.1016/J.CATENA.2021.105870

Zhang, Y., Zheng, R., Zhao, J., Ma, F., Zhang, Y., and Meng, Q. (2014). Characterization of H_3PO_4-treated rice husk adsorbent and adsorption of copper(II) from aqueous solution. *Biomed. Res. Int.* 2014, 1–8. doi:10.1155/2014/496878

Zhao, L., Hong, H., Fang, Q., Hei, H., and Algeo, T. J. (2023). Hydrologic regulation of clay-mineral transformations in a redoximorphic soil of subtropical monsoonal China. *Am. Mineral.* 108 (10), 1881–1896. doi:10.2138/AM-2022-8706

Zheng, H., Miao, C., Huntingford, C., Tarolli, P., Li, D., Panagos, P., et al. (2025). The impacts of erosion on the carbon cycle. *Rev. Geophys.* 63 (1), e2023RG000829. doi:10.1029/2023RG000829